Study of Protein-Small Molecule Interaction via Nanoaperture Optical Tweezer

by

Annie Yang-Schulz
B.Sc., University of British Columbia, 2021

A Thesis Submitted in Partial Fulfillment of the
Requirements for the Degree of

MASTERS OF APPLIED SCIENCE

in the Department of Electrical and Computer Engineering

We acknowledge and respect the Lək'ʷəŋen (Songhees and Xʷsepsəm/Esquimalt) Peoples on whose territory the university stands, and the Lək'ʷəŋən and W_SÁNEĆ Peoples whose historical relationships with the land continue to this day.

Study of Protein-Small Molecule Interaction via Nanoaperture Optical Tweezer

by

Annie Yang-Schulz
B.Sc., University of British Columbia, 2021

Supervisory Committee

Dr. Reuven Gordon, Supervisor
(Department of Electrical and Computer Engineering)

Dr. Makhsud Saidaminov, Academic Unit Member
(Department of Chemistry)

Supervisory Committee

Dr. Reuven Gordon, Supervisor
(Department of Electrical and Computer Engineering)

Dr. Makhsud Saidaminov, Academic Unit Member
(Department of Chemistry)

ABSTRACT

This thesis explores small molecule-protein interactions using nanoplasmonic optical tweezers. Since their inception by Ashkin, optical tweezers have been widely adopted in biology due to their unique ability to manipulate nanoscale objects. The transcriptional activity of a single RNA polymerase molecule has been measured using dual optical tweezers and DNA tethering, revealing key processes such as transcriptional stepping, pausing, backtracking, and termination. However, tether-free nanoscale trapping remains challenging with single-beam optical tweezers, as trapping forces decrease disproportionately with target size reduction. A major breakthrough occurred with the development of subwavelength apertures for field enhancement, enabling trapping of free solution single proteins. Our lab specifically employs double nanohole apertures to generate a highly confined gradient field, facilitating stable trapping at the nanoscale.

Abnormal protein phosphorylation plays a critical role in chronic illnesses such as Alzheimer's disease, cancer, and arthritis. Consequently, both kinase and phosphatase therapeutics have become major areas of research. While numerous kinase inhibitors have received FDA approval, phosphatase-targeting drugs have faced significant challenges due to difficulties in identifying effective and selective binding sites. This thesis explores a promising phosphatase-targeting cancer therapeutic candidate using subwavelength-assisted optical tweezers. We present qualitative insights into the structural impact induced by small-molecule binding, complemented by molecular dynamics simulations. Additionally, we quantify binding affinity at both the single-molecule and ensemble levels.

Contents

List of Tables

List of Figures

ACKNOWLEDGEMENTS

I would like to thank my supervisor, Dr. Reuven Gordon, for his knowledge, guidance, and the opportunity to work in the exciting field of plasmonics.

I would like to thank my fellow lab mates for their disucssions, encouragements and friendship. Matthew Peters, Sherin George, Keiran Letwin, Tianyu Zhao, Behnam Khosravi, Marlene Otto, and Peter Grant.

In addition, I would like to extend my gratitude to Cuifeng Ying, Saaman, Mahya, Yanhong, Maria, Satya, Anupam, and Zeynep for their wisdom and collaboration.

To my wonderfully kind, smart, and talented friends, thanks for the all the support you have generously given me.

To my family, thank you for the love and unwavering support to my adventures.

To my cats, Converse and Godiva, for their constant companionship and love.

One must still have chaos in oneself to be able to give birth to a dancing star.
Friedrich Nietzsche

DEDICATION

To Tyler.

Love is not consolation. It is light.

Chapter 1

Introduction

1.1 Motivation

The invention of the single-beam optical tweezer by Ashkin revolutionized the way we interact with and study microscopic particles. This technique has been widely adopted for investigating biological systems [1, 2]. A paramecium, a single-celled organism, was “grabbed" by the laser beam, allowing manipulation of its organelles, approximately 1 μm in size [3]. As research progressed from the microscale to the nanoscale, free-solution bovine serum albumin (BSA) proteins were successfully trapped with the aid of a nanoaperture[4]. Since the first report of single-protein trapping, continuous refinements in methodology and data analysis have expanded its applications. Each advancement illuminates the unknown, deepening our understanding of light-matter interactions, protein folding and unfolding, and fundamental biological mechanisms essential to life.

1.1.1 Direct Observation of Small Molecule Activator Binding to Single PR65 Protein

The combination of the ability to trap a single unmodified protein, the relationship between transmission and polarizability, and the sensitivity of optical tweezers makes this technique well-suited for studying structural dynamics induced either thermally or by an external binding agent [5, 6]. Single-molecule trajectories enable real-time observation of biological processes, providing a clear advantage over ensemble measurements, where dephasing, loss of synchronised behaviour of individual molecules, obscures the transient, dynamic behavior of individual molecules [7]. The current

landscape of single molecule binding kinetics measurement largely involves flourscent tagging [8]. A major issue with fluorescence-based methods is the concentration-dependent background noise, as the concentration of the tagged molecule increases and the background fluorescence rises, reducing the reliability of the signal. Using NOT, we explore the interaction of a cancer drug candidate designed to reactivate a phosphatase protein with its scaffold subunit. The time-series transmission signal, fitted to step functions using a Hidden Markov Model (HMM), reveals state transitions of the protein. Further analysis quantifies single-molecule binding kinetics.

1.1.2 Other Works: Rapid and Cost-Effective Fabrication of a Nanoscale Optical Trapping Microfluidic Chip

Proteins are often referred to as the “workhorses" of the cell, as they are central to nearly all cellular processes. With the median length of human proteins being 375 amino acids, a rough estimate suggests that the radius of human proteins is around 4 nm [9]. Techniques such as green fluorescent protein (GFP) tagging can be better characterized as forming protein complexes, since GFP itself has a comparable size to most proteins. The act of tagging may unintentionally perturb mechanisms of the protein of interest [10, 11]. In vitro studies of proteins close to their native environment provide a more accurate representation of their behavior and mechanisms. Given that NOT is well-suited for studying biomolecular interactions and processes, it is a natural progression to integrate a fluidic system for a more rigorous examination of the effects of ligand introduction, environmental changes, and other factors.

1.2 Agenda of this Thesis

Chapter 2 discusses the background and principles of optical tweezers and expands on the topics of subwavelength apertures and plasmonics. NOT and the developed characterization techniques are also presented.

Chapter 3 details the methods for nanoaperture fabrication, protein solution preparation, and trapping sample preparation. It also includes a description of the trapping setup and procedure.

Chapter 4 presents a case study on single-protein and small-molecule binding interactions as observed by NOT. The results in this chapter stem from collaborative

work, with the division of contributions stated under Author's Contribution.

Chapter 5 highlights two projects I worked on. First, a facile fluidic chip fabrication method designed for use with NOT is presented. Second, small-molecule binding interactions with a point-mutated form of the PR65 protein are discussed.

Chapter 6 concludes this thesis with a high-level summary and a discussion of future outlooks.

1.3 Author's Contribution

The work presented in Chapter 4 published as: Yang-Schulz, A., Zacharopoulou, M., Yilmaz, S.Z. et al. Direct observation of small molecule activator binding to single PR65 protein. npj Biosensing 2, 2 (2025). https://doi.org/10.1038/s44328-024-00018-7

A.Y.S. conducted the NOT experiments and analyzed the result. R.G. conceived the NOT experiment and supervised the experiment and analysis. M.Z. conducted the NanoDSF, NMR, and FP experiments and analyzed the results, and L.S.I supervised this work. S.S., A.B. and I.B. conducted and analyzed the docking simulations. I.B. supervised all docking simulations. S.Z.Y., M.G., and I.B. conducted and analyzed the MD simulations. M.G. and I.B. supervised all MD simulations. M.O. provided ATUX-8385 and provided experimental guidance on use. D.N. performed the NMR experiments and analyzed the results. A.Y.S., M.Z.,L.S.I., S.S.,S.Z.Y., A.B., M.G., I.B., and R.G. wrote the manuscript. All authors reviewed the manuscript.

Chapter 2

Background

This chapter begins with an overview of conventional single-beam optical trapping, focusing on the principles of optical forces. It then examines the limitations of this method, particularly when applied to nanoscale objects. To address these challenges, the discussion transitions to subwavelength apertures, exploring classical diffraction theory and the relationship between transmission and the ratio of particle size to wavelength. The chapter further introduces the phenomenon of extraordinary optical transmission and its connection to surface plasmons. Building on these concepts, it concludes with nanoaperture-assisted trapping, where a large gradient field generated enables effective nanoscale trapping.

2.1 Optical Trapping Forces

The invention of optical tweezers (OT) in 1986 by Arthur Ashkin won the 2018 Nobel Prize for Physics, his invention consisted of a single laser beam, focussed by a high numercial aperature objective, with a high gradient profile[12, 13]. Ashkin demonstrated the abilities of using a laser beam to grab and manipulate dielectric particles. Since then, OT has been applied for studies for cell biology, soft matter physics, nanotechnology et [14, 15, 16, 17]. To give an example of knowledge illucidated by the use of OT, motor protein kinesin attached to a dielectric bead was moved to a microtubule. The displacement of the kinsein was measured through the deflection of the laser beam. Through this, the step size of kinesin was measured to be 8 nm [18].

The working principle of OT is the conservation of momentum of photons. The forces exerted can be decomposed into a gradient and scattering force. With the

large gradient field, when a dielectric particle is placed off centre axis of the beam the particle experiences a net gradient force pulling the particle back towards the focus and central axis of the beam. Scattering force is along the direction of propagation. The summation of forces on the particle places it at the centre of the x-axis and slightly down stream from the beam waist (z-axis). If the particle is larger than the wavelength, $r \gg \lambda$, ray optics model can be used to describe the trapping forces . For particles in the Rayleigh scattering regime, $r \ll \lambda$, particle in a an external inhomogenous electromagnetic field can be modelled as a point dipole. Lorentz force states that the force experienced by a dipole in an electromagnetic field is given by [19]:

$$\mathbf{F} = (\mathbf{p} \cdot \nabla)\mathbf{E} + \left(\frac{d\mathbf{p}}{dt}\right) \times \mathbf{B} \tag{2.1}$$

where:

$$p = \text{polarization},$$

$$E = \text{electric field},$$

$$B = \text{magnetic field}$$

With a linear polarisation response to the external field, $\mathbf{p} = \alpha\mathbf{E}$ where α denotes polarisibility, Equation 2.1 can be re-written as:

$$\mathbf{F} = \alpha \left[(\mathbf{E} \cdot \nabla)\mathbf{E} + \left(\frac{d\mathbf{E}}{dt}\right) \times \mathbf{B}\right] = \alpha \left[\frac{1}{2}\nabla E^2 + \frac{d}{dt}\left(\mathbf{E} \times \mathbf{B}\right)\right] \tag{2.2}$$

The intenstiy of the laser beam is proportional to the sqaure of the amplitude of the electric field, E^2. With a Gaussian beam as depicted in Figure 2.1, the peak in intensity occurs at the center of the beam. The gradient dependent force draws the particle to the position of highest electric intensity. The gradient force is given as:

$$\mathbf{F}_{\text{grad}} = \frac{1}{2}\alpha\nabla E^2 \tag{2.3}$$

Assuming a spherical dielectric particle, the polarisiability is then [20]:

$$\alpha = \left(\frac{n_p^2 - n_m^2}{n_p^2 + 2n_m^2}\right) n_m^2 r^3 \tag{2.4}$$

where:

$$n_p = \text{refractive index of the particle},$$

$$n_m = \text{refractive index of the background medium,}$$

$$r = \text{radius of particle}$$

Scattering force arises from the attenutation of the light via absorption and scattering, the resulting rate of attenuation is described by the extinction cross section σ_{ext}. The constiuents of σ_{ext} is of absorption and scattering cross seciton. Scattering force, with Rayleigh approxmiation, can be written as:

$$\mathbf{F}_{\text{scat}} = \frac{n_m \sigma_{\text{ext}}}{c} \bar{\mathbf{S}}_{\mathbf{i}} \tag{2.5}$$

where:

$$n_m = \text{refractive index of the particle,}$$

$$\sigma_{\text{ext}} = \sigma_{\text{abs}} + \sigma_{\text{scat}},$$

$$c = \text{speed of light}$$

$$\bar{\mathbf{S}}_{\mathbf{i}} = \text{time averaged Poynting vector}$$

For small dielectric particles, $\sigma_{\text{ext}} \approx \sigma_{\text{scat}}$ as σ_{scat} dominates. As such, we can approxmiate the σ_{ext} as [20]:

$$\sigma_{ext} = \frac{128\pi^5 r^6}{3\lambda^4} \left(\frac{n_m^2 - n_b^2}{n_m^2 + 2n_b^2}\right)^2 \tag{2.6}$$

In conjunction with gradient force, the scattering force pushes the particle slightly downstream from the region of maximum intensity. Based on Equations 2.5 and 2.3, it can be deduced that the scattering force will drop off faster as the size of the particle decreases. For the scattering force, the force scales with both particle size and incident wavelength:

$$F_{\text{scat}} \propto \frac{r^6}{\lambda^4}$$

Whereas for the gradient force, it scales with the size of the particle as:

$$F_{\text{grad}} \propto r^3$$

Counteracting Force and Limitations to Conventional Optical Tweezers

To acheive stable trapping in liquid suspension, gradient force must counteract Stokes' drag and Brownian motion [21]. When a particle is supended in liquid or gas, the

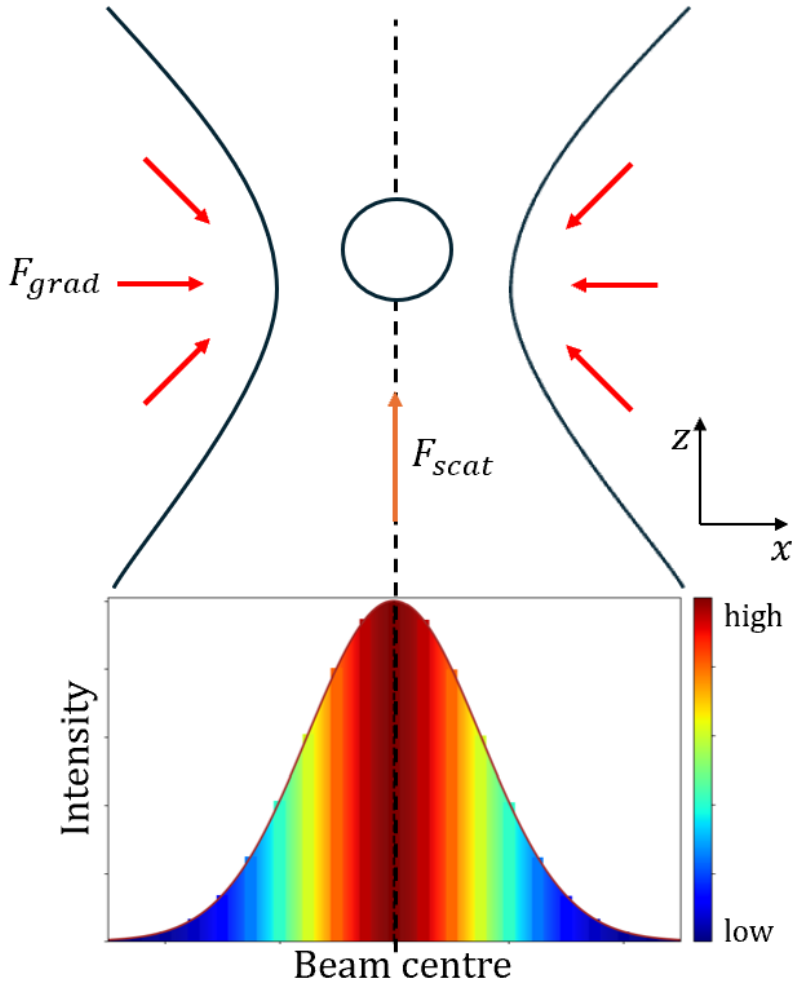

Figure 2.1: **Depiction of optical trapping forces** A tightly focussed single laser beam traps the dielectric sphere at the beam center through the graident force. Scattering force pushes the sphere slightly downstream, along the propagation direction of the beam, from the beam waist.

particle experiences irregular motion due to the bombardement of molecules in the medium. Brownian diffusivity is expressed by the Stokes-Einstein expression [22]. It is to note that as the particle size and viscosity of fluid decreases, faster the motion. Conversely, as the temperature increases, the higher the kinetic energy of molecules. This leads to faster motion.

$$D_B = \left(\frac{kTC_c}{3\pi\mu 2r} \right) \tag{2.7}$$

where:

$k =$ Boltzmann's constant,

$T =$ temperature (Kelvin),

$\mu =$ viscosity of fluid

$r =$ radius of particle

As the particle moves through a low Reynold's number fluid, a resistive force known as Stokes' drag is exerted on the particle. The force scales linearly with the radius of the particle.

$$\mathbf{F_{Stokes}} = 6\pi\mu r\mathbf{v} \tag{2.8}$$

where:

$r =$ radius of particle

$\mu =$ viscosity of fluid

$\mathbf{v} =$ flow velocity

As the particle size decreases, the scattering force diminishes rapidly, scaling as r^6, while the gradient force scales as r^3. In contrast, Stokes' drag decreases much more slowly with particle size, as shown in Equation 2.8. Therefore, to achieve stable trapping at smaller particle sizes, the gradient force must be enhanced—either by increasing the incident power or leveraging field enhancement through nanoapertures. Conventional optical trapping typically works with microscaled particles as stable trapping remains challenging [23]. Increasing laser power is not a viable solution due to potential thermal damage to the trapped object. This limitation is especially critical in biological applications, where optical tweezers are widely used. Maintaining an acceptable localized temperature at the trapping site is essential to prevent biological damage.

2.2 Subwavelength Aperture

Subwavelength optics refers to the study of interaction between the electromagnetic wave and object smaller than half the wavelength. In 1944, Hans Bethe published a theoretical model of electromagnetic wave diffraction through a subwavelength hole [24]. The problem he considered had the following setting: a subwavelength hole is cut from an infinite plane, negligbly thin, and perfectly conducting screen. Bethe's method was based on solving Maxwell's equations while enforcing continuity and boundary conditions. He introduced fictious magnetic currents and charges within the aperture to satisfy boundary conditions on the screen. The result of Bethe's theory states that the light diffracted from the aperture can be modeled as radiation from a magnetic dipole originating for the centre of the aperture. For plane waves normally incident from the left of the screen [25]:

$$P_{\text{transmitted}} = \frac{64}{27\pi} k^4 r^6 S_i = \sigma_{\text{eff}} S_i \tag{2.9}$$

where:

$$S_i = \frac{1}{2}\epsilon_o {E_i}^2$$

$$E_i = \text{incident electric field}$$

On the right-hand side of Equation 2.9, excluding S_i, is the effective cross-section of the physical hole, which has an area of πr^2. From the k^4 term and normalising to the area of the hole, it can be stated that the relation of power transmistted through a subwavelength aperture is:

$$T \propto \frac{r^4}{\lambda^4}$$

This results predict steep roll off in transmission as the size of the aperture continues to shrink. It is also to note that with an aperture of the same physical size, if the surrounding dielectric medium is changed to have a larger refractive index, this would effectively scale the transmission by Δn^4.

Although Bethe's theory provided a good model for the diffraction of light through subwavelength apertures, it did not account for surface waves that may play a significant role in certain cases. Specifically, the theory may underestimate the amount of light transmission when surface waves are involved, as they can contribute significantly to the transmission. This limitation became evident in 1998, when Ebbesen et al. reported experimental results that contradicted Bethe's classical diffraction

theory.

Findings from Ebbssen et al. showed extraordinarily high optical transmission—up to three orders of magnitude greater than predictions based on Bethe's theory—through subwavelength periodic hole arrays in metal films[26]. This discovery led to the emergence of a new field known as extraordinary optical transmission (EOT).

EOT refers to the enhanced transmission of light through subwavelength apertures in a metallic film, an effect attributed to the resonant excitation of surface plasmon waves. According to Bethe's 1944 diffraction theory, a subwavelength aperture should have a very small optical cross-section, resulting in significantly reduced transmittance. When surface waves are considered, the normalized transmittance (relative to the hole area) in periodic arrays can exceed unity. Since its discovery, EOT has found applications in metamaterials, plasmonic lenses, optical trapping, and various other fields of nanophotonics[27, 28].

2.3 Surface Plasmons

Surface plasmons (SP), induced by an external electromagnetic wave, are collective oscillations of electrons at the interface between a metal and dielectric. There are two categories of SP, one being surface plasmon polariton(SPP) and localised surface plasmons. SPs are confined to the metal-dielectric interface(does not radiate outward from it), they exhibit evanscenet decay perpendicular from the interface[29, 30]. Penetration depth of SPs are typically of tens to a few hundred nanometers. This strong confinement of field leads to a large field enhancement. Additionally, the SP wavelength is shorter than the free space wavelength, the shorter wavelength than allows for a smaller focus. SPPs propagate along the surface of the interace. As it propagates along the surface, it loses energy from the evanecent wave in the direction perpendicular to the interaface. SPPs cannot be excited with free space excitation due to momentum mistmatch. In free-space excitation condition, the incident beam wave vector is less than the SPP wavevector. Configurations such as the Otto, Kretschmann geometry are typical wavevector enhancement methods for generation of SPPs. Contrary to SPPS, localised surface plasmons(LSP) are SPs confined to a small, typically subwavelength, geometry. Unlike SPPs, LSPs can be excited by direct illumination because the curved surface exerts an effective restoring force on the displaced electrons, leading to resonance and field amplification both inside the aperture/nanoparticle and in the near-field zone surrounding it.

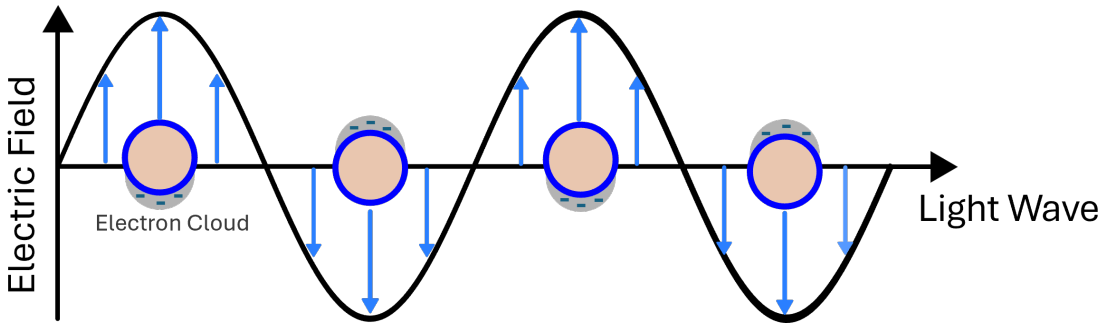

Figure 2.2: **Localized Surface Plasmon (LSP) Resonance.** Collective oscillation of conduction electrons induced by an external electromagnetic field. The resulting localized field enhancement occurs near the nanoparticle surface.

2.3.1 Nanostructures: Plasmonic Assisted Trapping

To generate high-gradient fields in nanoscale volumes for nanoparticle trapping, metallic nanostructures are typically fabricated on dielectric substrates. When surface plasmon conditions are satisfied, LSPs are confined and focused at the sharp features of the nanostructure. This results in minimal energy loss due to rapid adiabatic nanofocusing and electrostatic lightning rod effects [31, 32]. These field enhancements can reach several orders of magnitude and can occur even off resonance, albeit with comprise of field enhancement[33, 34]. LSP-assisted traps, commonly referred to as plasmonic traps, have been realized using various topological designs, including single and double nanoholes, bowties, and C-shaped geometry[35, 36].

In our group, we focus on the double nanohole geometry, where field amplification occurs specifically at the cusps of the nanoholes.

2.4 Self Induced Back Action

In Ashkin's pioneering work, he states stable trapping requires the trapping potential well to have a depth of around $10k_BT$ to counteract stochastic motion [12]. Juan et al. demonstrated and proposed a dynamic approach to reconfiguring the trapping potential. In this approach, the trapped object actively modifies the trapping force as it moves in and out of the metallic nanoaperture [37]. Since the transmission of nanoapertures is highly sensitive to changes in the surrounding dielectric medium, the presence of a dielectric object alters the effective refractive index, leading to a shift in

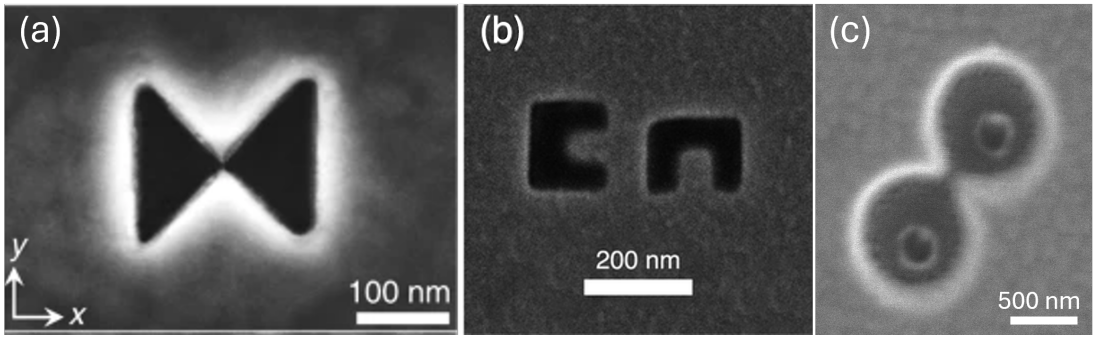

Figure 2.3: **Plasmonic trapping nanoapertures** a) Bow-tie geometry, reproudced from ref. [35] b) C-shaped geometry, reproduced from ref. [36] c) double nanohole aperture

transmission. If the object has a higher refractive index than the background buffer, this results in a sudden increase in transmission. This change effectively deepens the trapping potential well. If the object begins to move away from the trapping site, the photon momentum passing through the nanoaperture decreases. According to Newton's third law of motion, this change induces a reactionary force that directs the particle back toward the trapping site. With the SIBA force, particles can be stably trapped using up to 20 times lower optical intensity than without.

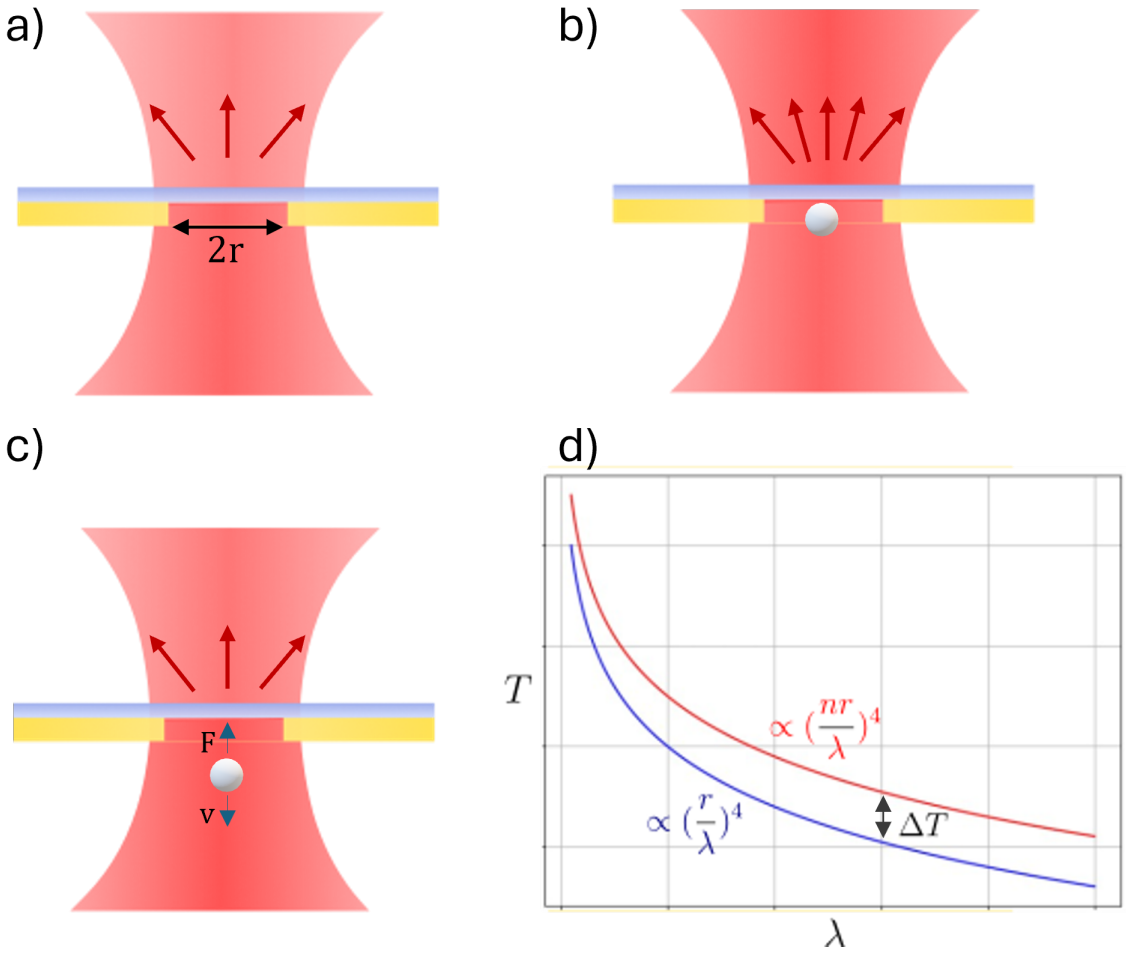

Figure 2.4: **Optical transmission through a subwavelength aperture with SIBA affects** a) incident laser beam onto an unloaded aperture. b) Particle enters trap, leading to enhanced transmission due to modfied effective refradice index. c) Particle moves away from trap leading to a decrease in transmission and increase in restoring force. d) Red shift and an increase in transmission is associated with dielectric loading of the aperture.

2.5 Nanoaperture Optical Tweezer

With the effects of field enhancement through surface waves and SIBA, stable trapping of nanoparticles have been acheived since over a decade ago. One of the prominent breakthroughs came from Pang and Gordon in 2012 where a single protein was trapped using a DNH aperture[4]. Since then, single proteins have been consistently trapped and studied.

For our group, we specialize in using DNH aperture for trapping, DNH can be easily integrated into a conventional single beam trapping system placing the DNH sample with trapping solutions between the condenser and objective, this is described in full in the subsequent chapter. DNH localizes high field enhancement in the confines of 10s of nanometers. Finite difference time domain (FDTD) simulation results of DNH with varying cusp seperation showed field enhancement of over 10^2 in magnitude (Figure 2.5)[38]. As object of interest are often biological in nature, heating affects at the trapping site have been investigated by several groups experimentally and simulation-wise. For our system, a linear relationship between laser power and temperature change were determined to be 0.64 K/mW [39, 6]. Hence, at 20 mW of trapping power, sufficient for single protein trapping, the local temperature is approxmately 35 $°C$. The trapping power dependence of the trapping site allows for the study of thermal effects to biological systems.

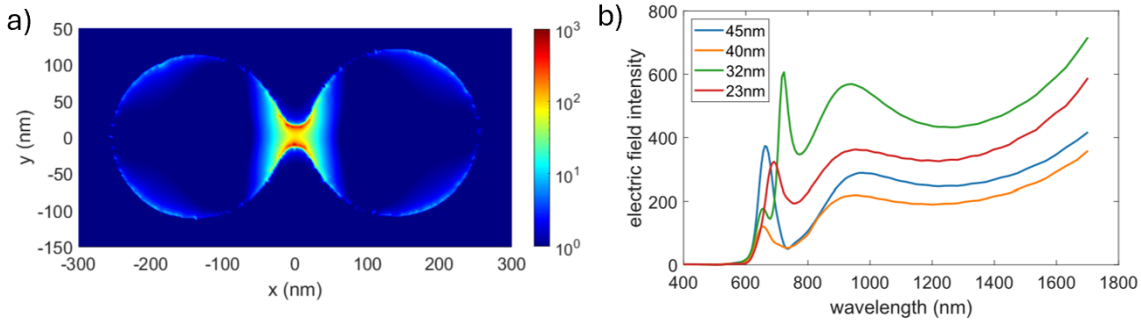

Figure 2.5: **FDTD simulation of field enhancement from a DNH, figure adapted from [38]** a) Visualisation of field enhancement inside the aperture with 32 nm cusp seperation. b) Normalised electric field enhancement versus wavelength for varying cusp size

2.5.1 Standard Characterziation Techniques

There are three standard techniques used for characterising trap stiffness and particle size. Namely, they are of corner frequency and normalized root mean sqaure deviation.

Trap Stiffness through Power Spectral Denisty Anaylsis

Langevin equation can be used to describe a trapped particle[40, 41, 42]:

$$m\frac{d^2x(t)}{dt^2} = -\gamma\frac{dx(t)}{dt} - kx(t) + \sqrt{2k_BT\gamma}W(t) \tag{2.10}$$

where:

$$m = \text{particle mass},$$

$$\gamma = 6\pi\mu r; \text{Particle friction coefficient, determined by Stokes' laws},$$

$$k = \text{optical trap stiffness},$$

$$k_B = \text{Boltzmann's constant},$$

$$T = \text{Absolute Temperature (Kelvin)},$$

$$W(t) = \text{Wiener process, term accounting for Brownian motion}$$

Equation 2.10 is of 1-dimension, the same formulation can be applied to y(t) and z(t) to describe a 3D optical trap. As most trapping experiments are conducted with particles suspended in liquid with low Reynolds number, the intertial term can be assumed to zero. As such equation 2.10 can be simplified to the overdamped Langevin equation:

$$\frac{dx(t)}{dt} = -\frac{2\pi}{\tau}x(t) + \sqrt{2D_B}W(t) \tag{2.11}$$

where:

$$\frac{1}{\tau} = \frac{k}{\gamma}$$

τ represents the autocorrelation time constant. The term $\frac{1}{\tau}$ describes the time scale for which the restoring force acts, this is in relation to the trapping stiffnes k and drag. Corner frequency, -3 dB point of the power spectral density, is equals of the inverse of the $2\pi\tau$:

$$f_c = \frac{k}{2\pi\gamma} \tag{2.12}$$

By taking the sqaure modulus of the Fourier transform of Equation 2.11) gives

the power spectral density of the particle motion. Equation 2.13 is of a Lorentizan form and f_c can thus be calculated by fitting the $P(f)$ with a Lorentizan fit.

$$P(f) = |X(f)|^2 = \frac{A}{f_c^2 + f^2} \tag{2.13}$$

where:

$$A = \frac{D_B}{(2\pi)^2}$$

It should be noted that due to the presence of thet DNH nanostructure boundries, the normal friction coefficient $\gamma_\perp$ of Stokes' drag can be modulated as Equation 2.14 [43]. The presence of nanoaperture walls leads to an increase in drag force, and a decrease in the distance to the surface further increases the drag.

$$\gamma_\perp = \frac{6\pi\mu r}{1 - \frac{9r}{6h}\frac{r^3}{8h^3} - \frac{45r^4}{256h^4} - \frac{r^5}{16h^5}} \tag{2.14}$$

where:

$$h = \text{distance to the wall in reference to the particle centre}$$

Tranverse component of the friction coefficient is likewise modified due to the added boundaries. However, this is not as well defined as per $\gamma_\perp$.

Protein Sizing via RMSD

Wheaton and Gordon demonstrated that the transmission intensity of an optical trap can be used to characterize the molecular weight of single proteins[44]. Utilizing NOT, six size-standard proteins were trapped. Analyzing the root mean sqaure deviation (RMSD) of their transmission signals revealed a linear dependence on molecular weight, which can be explained as follows. The potential energy of a Rayleigh particle, under the dipole approximation, can be written as:

$$U = \frac{1}{2}\alpha E^2 \tag{2.15}$$

The intensity transmitted through the nanoaperture is proportional to the potential energy of the particle. Therefore, the RMS of the intensity signal is similarly proportional:

$$\sqrt{I^2} \propto \sqrt{U^2} = \alpha \sqrt{\frac{|E|^4}{4}} \tag{2.16}$$

According to Equation 2.16, the transmission signal intensity scales with the particle's polarizability. Since polarizability scales with particle volume, and assuming constant mass density, an approximately linear relationship between RMSD and molecular weight is expected.

2.6 Concluding Remarks

This chapter provided an overview on the principle of optical trapping and limitations in a convential single beam optical trap. A discussion of Bethe's theory and EOT to discuss light transmission through a subwavelength aperture followed. With the intergration of subwavelength aperture to single beam optical trap, barriers to stable trapping of a nanoparticle were broken through. Additionally, we review the standard characterization techniques to NOT.

Chapter 3

General Methodology

This chapter details methods conducted for the experiments included in this thesis. For nearly a decade, our lab has transitioned from fabrication of DNH aperatures using Focused Ion Beam (FIB) milling to collodial lithography. The collodial lithography approach is cost effective and produces higher throughput. Additionally, we will discuss how trapping solutions and samples are made.

As a summary, this chapter will be comprised of the following subsections:

- Collodial lithography fabrication of DNH
- Trapping solution and sample preparation
- Optical trap setup and trapping procedure

3.1 DNH Fabrication

For nearly a decade, our group has utilized colloidal lithography for the fabrication of DNH apertures. Prior to this, FIB milling was the primary method. The transition to colloidal lithography enabled higher throughput at significantly lower costs. By varying the plasma etching time or power, the dimensions of polystyrene (PS) spheres can be fine-tuned for optimized nanoparticle trapping [45].

3.1.1 Colloidal Lithography

Using a diamond scribe, a microscope slide with dimensions $75 \times 50 \times 1$ mm is divided into three roughly equal sections. The slides are then placed in an ethanol bath for

sonication. After 10 minutes of sonication, the slides are rinsed sequentially with acetone, isopropanol, and ethanol, followed by blow-drying with nitrogen gas.

Next, approximately 1 mL of ethanol is mixed with a specified volume of PS bead solution. The required volume depends on the brand of PS beads: typically, 15–20 μL for ThermoFisher and around 6–7 μL for Sigma-Aldrich. The ethanol and PS bead mixture is gently mixed to be a homogeneous solution. The suspended PS beads are used to form a mask.

Using a micropipette, 10 μL of the solution is distributed onto the slide in a zig-zag pattern. The slides are left overnight in a glass petri-dish for the ethanol to evaporate. To shrink and fuse the PS dimers, a plasma cleaner (Harrick Plasma PDC-001) is used at the "HIGH" power setting, with 30W applied to the RF coil. The etching time is brand-specific; for ThermoFisher 300 nm PS beads, the relationship between etch time and cusp size is shown in Figure 3.1. For better consistency in aperture dimensions, each slide should be plasma etched individually under identical placement, power, pressure, and gas flow conditions. It may be of advantage to intergrate Harrick Plasma PlasmaFlo to the existing plasma cleaner to be able to control the flow rate, vaccum pressure quantatively.

Using the MANTIS QUBE sputtering deposition system, 7 nm of Titanium is sputtered on first to act as an adhesion layer between the glass substrate and gold layer. Although our group uses Titanium exclusively as an adhesion layer, materials such as chromium trioxide and chromium can also act as adhesion layer for different heat absorption properties. To do so, the slides are mounted onto the sample stage of the deposition system with double sided tape. The side without the mask is adhered onto the stage. Instructions for operating the system are followed to sputter the 2 layers of material. The titanium layer is sputtered on first with gold following suit upon completion. Studies have suggested that both the adhesion and gold layer play a pivotal role in the local temperature at the nanoaperature [46].

To remove the PS beads, the samples are placed in an ethanol bath and sonicated for 7 minutes. Characterization of the final product is discussed in the following section. There are cases where sonication does not remove the PS beads, if so, scotch tape can be used as an alternative method. However, the adhesiveness of the tape must be significantly reduced by repeatdely sticking and peeling the tape of a clean pair of nitrile gloves (or other clean surfaces) prior to gently sticking and removing the tape onto the sample slide. This method carries risk of peeling off the sputtered on layers and surface roughening.

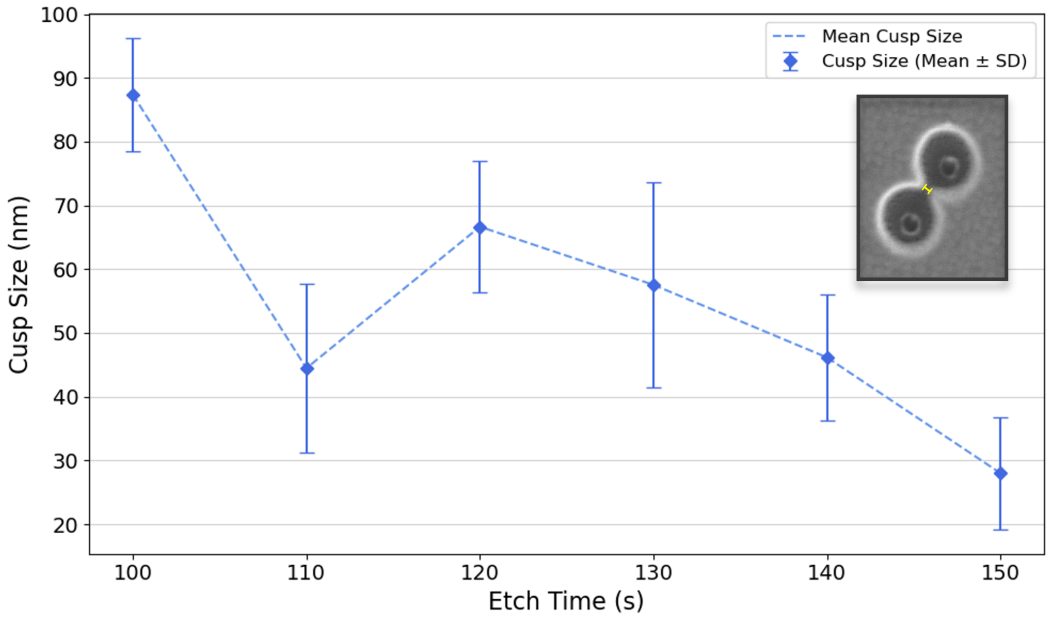

Figure 3.1: **Cusp size versus etch time for ThermoFisher 300 nm PS beads.** A general linear trend shows that increasing etch time results in a decreased cusp size. The initial rise in cusp size at 120s, as compared to cusp sizes obtained at 110s etch time, is likely to have originated from surface reflow between PS beads. The inset shows an SEM image of a double nanohole with a cusp size of 15.3 nm after 150 s of etching.

Characterization

Hitachi S-4800 Scanning Electron Microscope (SEM) was used to characterize the samples fabricated. The samples are imaged under the parameters of 8 mm working distance, 10 kV emission current and an accelerating voltage of 2 kV. Diameters, cusp seperation of the randomly distributed DNHs are measured to ensure the suitablity for the desired nanoparticle trapping. SEM images of a sample is shown on Figure 3.3. Further anaylsis can be conducted by use of Energy Dispersive X-Ray Spectroscopy (EDX) to anaylze elemental distribution of the fabricated sample. EDX is a non-destructive analytical technique based on unique electromagnetic emission spectrum from an atom upon X-ray excitation of the sample.

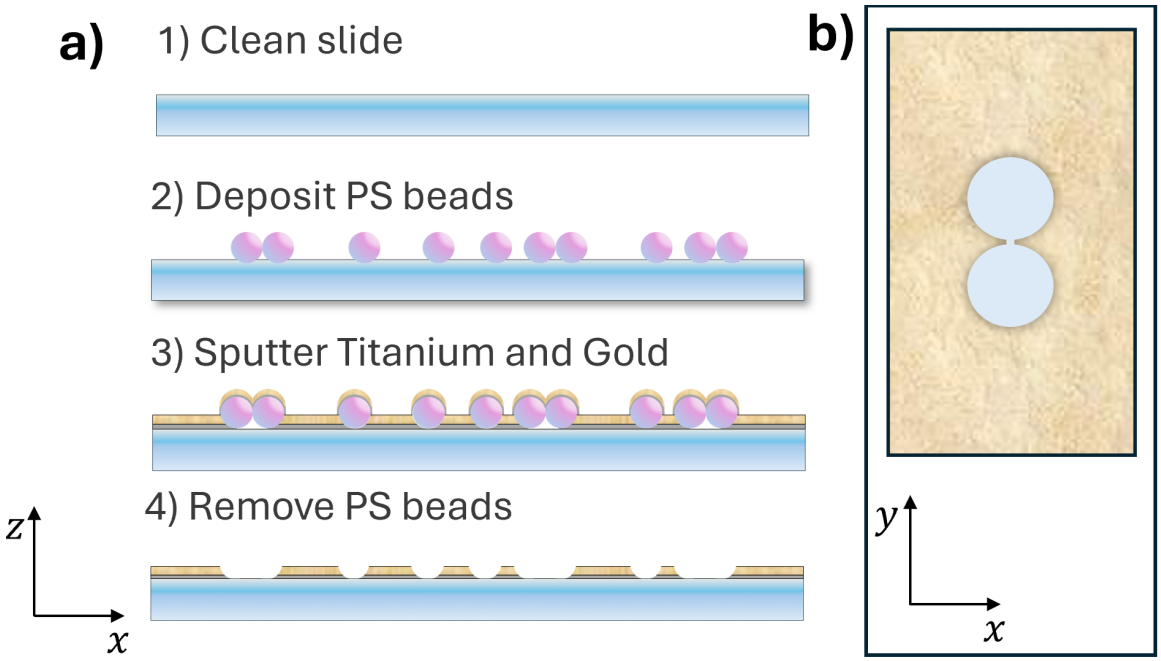

Figure 3.2: **Overview of DNH fabrication a) DNH fabrication via collodial lithography.** The mask is formed by depositing PS beads onto the glass substrate. A 7 nm thickness of Titanium and 70 nm thickness of Gold is sputtered onto the substrate. The mask is then removed via sonication as the final step. **b) Top-down view of a cartoon represenation of a DNH.**

3.2 Protein Solutions

Size standard proteins, Bovine Serum Albumin, Carbonic Anyhydrase and Cytochrome C, are aliquoted by mixing 1 mg of protein with 1 ml of phosphate buffered saline (PBS).

3.3 Trapping Sample Preparation

To prepare a trapping sample, a coverslip 24×60 with thickness 0.16 to 0.19 mm is rinsed respectively with acetone, IPA, and ethanol. The coverslip is then blow dried with nitrogen gas and placed onto a lens paper. An image spacer (Grace Bio-Labs GBL-654008-100EA) is adhered to the coverslip by removing the protective film from one side to expose the adhesive layer. Gently dab the corners of the spacer to ensure a secure bond. Remove the remaining protective film and add in 8 μL of trapping solution. Secure the microwell by placing a DNH slide directly onto the spacer. A

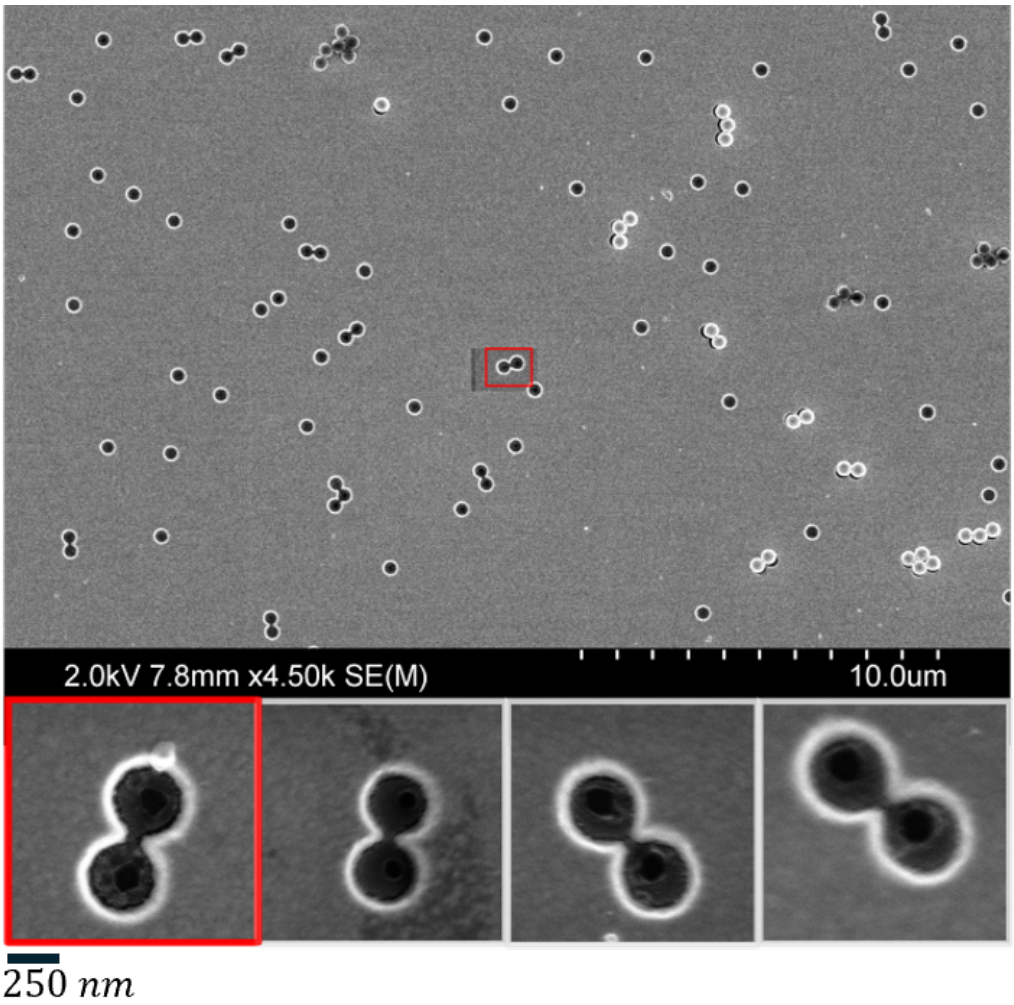

Figure 3.3: **SEM Imaging of DNH Sample.** The sample contains a decent amount of DNH structures. Due to random deposition, single, double, triple, and quadruple nanoholes are present. Most polystyrene beads were removed through sonication, though some remain on the sample. The red rectangular outline highlights a double nanohole in the zoomed-out image. A zoomed-in, rotated version of the same DNH is shown at the bottom left.

3D render of a trapping sample is depicted in Figure 3.4.

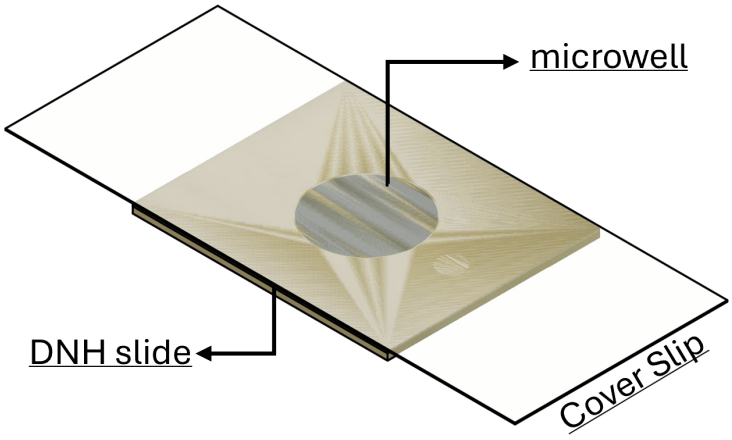

Figure 3.4: **3D Rendering of a Trapping Sample.** A typical trapping sample consists of three layers: a DNH slide, an image spacer, and a coverslip. The image spacer creates a microwell to hold the trapping solution.

3.3.1 Optical Trapping Setup

The optical trapping setup can be dissected into two portions, a vertical and horizontal column. In the horizontal column, a 980 nm fiber-coupled laser, collimated with a Thorlab FiberPort PAF2P-11E, is aligned to propagate through a linear polarizer and half wave plate. The two aforementioned components are used to control the polarization of the beam, this aids in distinguising double from single nanoholes based on DNH's transmission polarization dependence [45]. The beam is expanded and re-collimated to overfill the back aperature of the 100× oil immersion objective. Before the beam travels into the vertical column, a short-pass dichroic mirror is used to allow the laser beam to be reflected onto the vertical column and allow white light to be transmistted to a charge-coupled device (CCD) camera. Two mirrors are used to ensure that the beam travels center and through the vertical column. The 100× oil immersion objective focuses the laser and gets re-collimated by the 10× condenser. Note, between the objective and condenser sits a sample holder that is connected to

a piezeo-controller attached 3-axis translation stage. The beam then passes through a second short pass dichroic mirror. At the top of the vertical column sits the white light source. The reflected beam is focussed onto an avalanche photodiode (APD). Optical density filters are added onto the APD to ensure that the upper-limit of the unit is not reached. Figure 4.8 depicts a simplified setup.

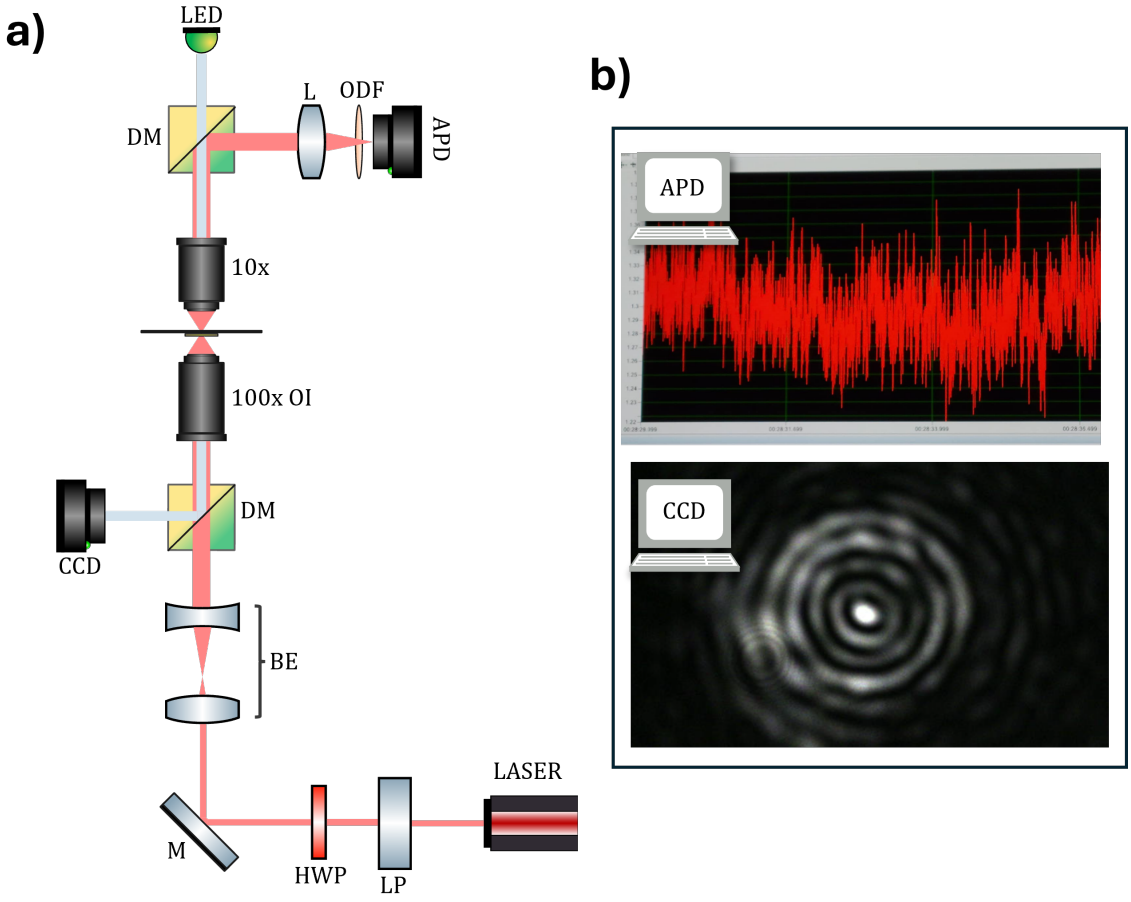

Figure 3.5: **a) Simplified optical trapping setup.** LP: linear polarizer; HWP: half-wave plate; M: mirror; BE: beam expander lenses; DM: dichroic mirror; CCD: charge-coupled device; 100× OI: 100× oil immersion objective; L: lens; ODF: optical density filter; APD: avalanche photodiode. **b) Monitor display of APD and CCD signals.** The DAQ software shows the real-time signal received from the APD. The sample screenshot captures a trapped protein undergoing conformational changes. The CCD camera displays laser fringes; when a nanoparticle approaches the trapping site, the fringes are perturbed, revealing the protein's path to the DNH.

Trapping Procedure

- Turn on the table pump to float the table, turn off the pump once a click is heard. It is to note that a floated table may be crucial to the efficiency and succuess of a trapping experiment.
- Add a drop of immersion oil under the image spacer from the coverslip side. Place sample onto the sample holder.
- Turn LED source on to illuminate the sample. Using the z-axis knob, focus the sample. The holes should be visible on the monitor screen that the CCD camera is attached to.
- Using the x, y axis knob, identify a potential DNH. DNHs appear brighter and slightly elongated, when compared to single nanoholes, on the camera.
- Turn on the laser, set current to be approximately 30 to 50 mA. Coarsely align the laser beam onto the potential DNH.
- Start acquisition on the DAQ software.
- Slightly under the focus the laser to maximize transmitted signal.
- Use the APT USER software, piezeo controller software, to finely adjust the posistion of the stage. Maximize transmission with all 3 axis.
- Rotate the half waveplate to verify if the aperature is a DNH. If the hole is single, there would be minimal changes in trasmission associated with the change of polarization. Sharp changes are expected with a DNH. If its a DNH, increase the power output of the laser for trapping. If not, return to item 4 and repeat the process.
- Wait for a transmission, noise change when a nanoparticle becomes trapped in the aperature. Generally, a trap can be characterized by a sharp change in transmission as well as an increase in the signal width.

3.4 Data Acquisition

Data is acquired at a sampling rate of 100 kHz using an Advantech USB-4711A data acquisition unit. The associated software, Advantech DAQ Data Logger Express, is

used for real-time display of the scattering signal from the sample. Data is exported from the same software for further analysis.

3.5 Concluding Remarks

This chapter presented a walkthrough of colloidal lithography fabrication of DNHs, protein preparation, trapping sample preparation, and trapping procedures.

Chapter 4

Direct observation of small molecule activator binding to single PR65 protein

4.1 Introduction

PR65, the scaffolding subunit of the serine/threonine protein phosphatase 2A (PP2A) family, provides a platform for the assembly of this heterotrimeric complex [47]. PP2A plays a critical role in regulating cell proliferation, maintaining cellular homeostasis and orchestrating cellular signaling pathways [48, 49]. Dysregulation of PP2A has been linked to various cancers and chronic conditions such as Alzheimer's disease and chronic obstructive pulmonary disease, thus presenting itself as a target for therapeutic intervention[50, 51, 52, 53, 54]. Reactivation of PP2A through a small-molecule activator of PP2A (SMAP), such as ATUX-8385, has shown to decrease hepatoblastoma and neuroblastoma cell proliferation *in vitro* and in animal models [55]. The aforementioned SMAPs are of the tricyclic sulfonamide class and bind directly to PR65, the subunit A of the trimeric PP2A. PR65 itself comprises 15 α-helical HEAT repeats. The HEAT repeats of PR65 form an elongated curved structure, with one helix from each repeating forming the outer, convex surface, and the other forming the inner, concave surface onto which the regulatory (B) and catalytic (C) subunits assemble. These SMAPs have been reported to drive conformation changes that subsequently promote heterotrimer formation [56]. Mechanistically, the ligand-induced conformation change is analogous to mechanical extension or compression [57, 56].

The structural impacts of ATUX-8385 on PR65 upon binding allow for a deeper understanding of the activation mechanism. Furthermore, for safety, efficacy and duration of response, it is important to understand the binding kinetics of any small molecule drug candidate.

While there have been a variety of techniques employed to study the structural changes and binding kinetics of small molecules with proteins, here we focus on nanoaperture optical tweezers. NOTs allow for studying single proteins and their interactions without the need for modifications, such as labels or tethers [4, 58, 59]. Here we use a double-nanoholes for generating a large gradient force capable of holding onto nanoparticles [45, 37]. More generally, shaped nanoapertures have been used in the optical tweezer field for the study of small biomolecules and other nanoparticles[60, 61, 62, 63, 64, 65, 37, 66, 67, 68, 69, 70]. The first report of trapping of a single protein demonstrated the technique's sensitivity by observing the conformational changes in bovine serum albumin (BSA) via changes in light transmission intensity as measured by an APD [4]. Integration of NOT with a nanopore further supports single protein trapping [68, 71, 72] and has been used to probe the interaction of antibodies with immunotherapy-relevant ligands [73].

Conformational changes were suggested from the NOT signal changes for two different types of proteins: $\beta-amylase$ and heat-shock protein 90 (HSP90) [74]. Iron ion loading and unloading of a single ferritin was observed by seeing structural changes in real-time using this technique [5]. Recently, we have used NOTs to study the impact of point mutation on the conformational behavior of PR65 [75], showing correlation between the extension of the protein observed in the optical scattering signal of the NOT and those predicted from molecular dynamics (MD) simulations.

The goal of the present study is to use NOTs to probe the interaction of a single PR65 protein with the clinically-relevant experimental small molecule ATUX-8385. We performed binding assays under equilibrium conditions and observed biomolecular dynamics in real-time. By tracking ligand-induced conformational changes and subsequently discerning the optical scattering signal into binary states, bound and unbound, dissociation and association rate constants can be determined through the "bound" time and "unbound" time. This is similar to single-molecule Förster resonance energy transfer (FRET), however, the ligand concentration is not limited to the typical nanomolar range as we are not hindered by background fluorescence noise by looking directly at the polarizability change of a single protein [7].

Previously, NOTs have been used to quantify established protein-drug interac-

tions, human serum albumin with tolbutamide and with phenytoin, obtaining dissociation constants within the previously reported range of values [58]. NOTs were also used to study strong interactions where the binding was essentially irreversible on the timescale of observation, e.g., biotin with streptavidin and acetylsalicylic acid with cyclooxygenase 2 [76]. Here we apply and extend the technique to a much less understood binding pair, to understand the binding kinetics and to observe the conformational changes induced upon binding.

In addition to NOTs, we use several techniques to investigate the binding characteristics and effects of SMAP ATUX-8385 to PR65. These include all-atom MD simulations, nano differential scanning fluorimetry (nanoDSF), nuclear magnetic resonance (NMR) and fluorescence polarisation anisotropy. In terms of molecular simulations, we explored the effect of ATUX-8385 binding on the structure and dynamics of PR65 by docking simulations followed by microseconds long MD runs, as well as microseconds simulations for apo PR65. Our docking simulations revealed a binding region that encompasses the inner helices of the HEAT repeats 4 and 5 (4_i and 5_i) and the outer helices of HEAT repeats 5 and 6 (5_o and 6_o). ATUX-8385 showed stable binding at this site throughout the 704 ns long triplicate MD runs of MD simulation, totaling 2.112 μs in combined trajectory length. ATUX-8385 binding stabilised an extended conformation in two runs and a compact form in a third run. The latter transitioned to the extended form towards the end of the 704 ns simulation, indicating the stabilising effect of ATUX-8385 bound to PR65, and its tendency to favor the extended conformation. NanoDSF showed that the presence of ATUX-8385 stabilised PR65 through increase in the melting temperature. NMR confirmed the binding of ATUX-8385. Fluorescence polarisation anisotropy experiments provided an ensemble dissociation constant in close agreement with the single molecule dissociation constant.

4.1.1 Protein Phosphatase 2A

In a cell, nearly one-third of proteins are regulated by phosphorylation and dephosphorylation, processes essential for functions such as cell cycle progression, enzyme activation, and protein-protein interactions [48]. Opposing kinases, phosphatases drive the cell into a dephosphorylated state. As PP2A is repsonsible for over 50% of Ser/Thr dephosphorylation, dysregulation and inhibition of the holoenzyme activity has been well-linked to cancer and neurodegenerative diseases [77]. Inhibition of

PP2A can be caused by marine toxin okadaic acid, deletions of holoenzyme encoding genes in various forms of cancer [78, 79, ?]. Further, hyperphosphorylated aggregate of tau proteins, hallmark of neurodegeneration, are mainly targeted by PP2A. *In vivo* studies has shown inhibition of PP2A results in tau pathology and cognitive impairment consistent of Alzheimer's disease [80, 81].

PP2A accounts for nearly 1% of total cellular protein [82]. Its core complex consists of a scaffolding subunit (A) and a catalytic subunit (C), each of which has two isoforms. The regulatory subunit (B) is more diverse, comprising four distinct families of isoforms. This diversity allows PP2A to regulate a broad range of cellular functions. The specific regulatory B subunit bound to the core complex determines the functional specificity of PP2A [83].

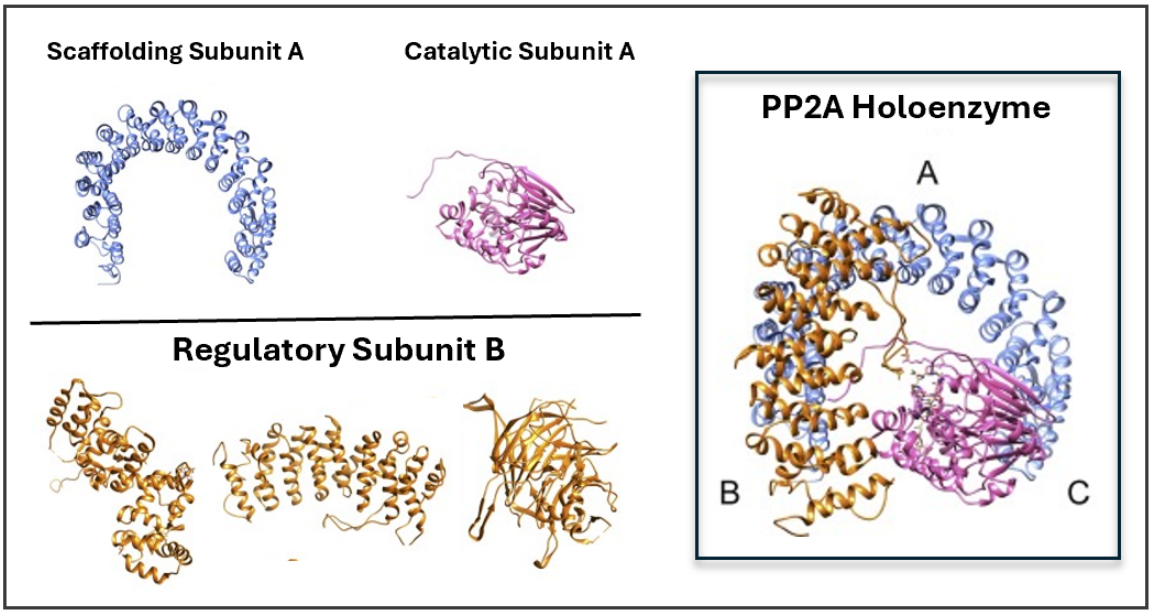

Figure 4.1: **Protein Protein Phosphatase 2A and its three constituents** PP2A holoenzyme is composed of scaffolding subunit A, catalytic subunit C and regulatory subunit B. Figure adapted from ref. [84].

4.1.2 In-Vivo and In-Vitro Study of PP2A Reactivation with SMAP

With the global rise in liver cancer, developing effective treatment methods to improve patient prognosis remains an active area of research [85, 86]. Only 5% to 15% of

patients, primarily those in the early stages of the disease, are eligible for hepatectomy [87]. For later-stage patients, treatment options include chemoembolization, in which the blood supply to the tumor is blocked shortly after the administration of anti-cancer drugs at the tumor site. Additionally, oral kinase inhibitors are commonly used for late-stage patients [88, 89]. However, long-term use of kinase inhibitors presents challenges such as toxicity and reduced efficacy due to drug resistance [90]. Notably, only one-third of patients experience meaningful improvements from treatment.

In 2023, Bownes et al. published a study on PP2A reactivation using two tricyclic sulfonamide-class compounds, ATUX-8385 and 3364, and their effects on hepatoblastoma [55]. The study investigated the human hepatoblastoma cell line HuH6 and a human hepatoblastoma-derived xenograft both in vitro and in vivo. After 24 hours of treatment with ATUX-8385 and 3364, PP2A activity increased, and immunoblotting revealed decreased expression of CIP2A, a cancerous inhibitor of PP2A. With PP2A reactivation, cancer cell proliferation significantly decreased in both the murine model and in vitro after just 24 hours of small-molecule treatment.

Given the promising results of this study and the growing interest in PP2A-targeted therapeutics, we aim to further investigate interactions between PP2A and SMAP. As the two SMAPS studied were designed to bind directly to the scaffold subunit. We focus the study between the interaction between PR65 protein and ATUX-8385. It should be acknowledged that the interaction between isolated PR65 protein and SMAP may not fully reflect the behavior of the holoenzyme in response to small molecule drugs. However, in the absence of the B and C subunits, such experiments can still provide valuable insights into the mechanics of PR65 that might otherwise be obscured.

In our experiments, monomeric PR65 was obtained using size exclusion chromatography (SEC). SEC separates molecules based on their molecular weight, allowing monomers, dimers, and oligomers to be resolved. Briefly, the protein solution passes through a column packed with a porous matrix that acts as a molecular sieve. Molecules larger than the exclusion limit remain in the mobile phase and elute earlier, while smaller molecules enter the pores and elute later in separate fractions. Detailed procedures for PR65 expression and purification are provided in the Methods section.

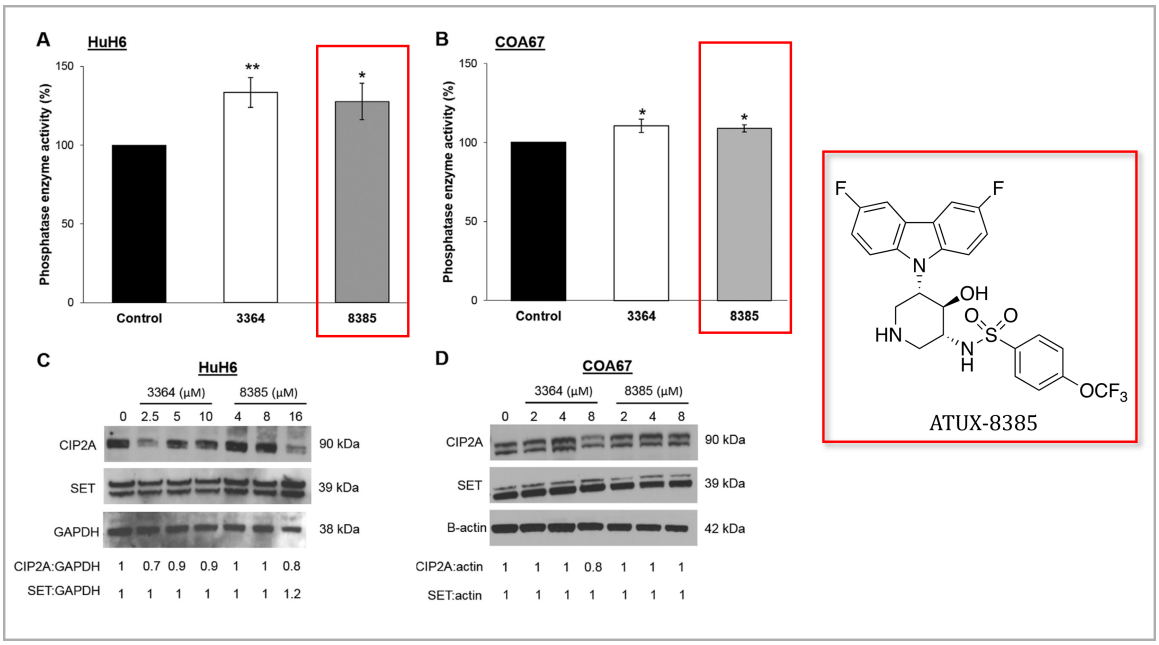

Figure 4.2: **In-vitro and In-vivo study of PP2A re-activation with SMA** a) For HuH6 and COA67 cell lines, treatment with two tricyclic sulfonamide compounds, 8385 and 3364, for 24 hours led to a notable increase in PP2A activity. b) Cancer cell proliferation was drastically decreased with 24 hours of SMAP treatment. Figure reproduced from [55].

4.1.3 Molecular Simulations

Molecular dynamics simulation is a computational method used to investigate the physical movements and interactions of atoms and molecules [91]. This approach can complement experimental techniques by providing an atomistic view of intra- and intermolecular interactions. For example, MD simulations can help interpret data from NMR, isothermal titration calorimetry (ITC), and optical tweezer experiments [92, 75]. In general, MD simulations aim to numerically solve a series Newton's equations of motion, allowing valuable insights to a time "evolution" of molecular movements (equation 4.2) [93].

$$f_i = m_i \ddot{r}_i = \frac{\partial}{\partial r_i} \mathcal{U} \tag{4.1}$$

where:

$$f_i = \text{force acting on atom } i,$$

$$r_i = \text{Position of atom i,}$$

$$m_i = \text{mass of atom i,}$$

$$\mathcal{U} = \text{potential energy}$$

For non-bonded interaction atomic interactions potential energy $\mathcal{U}$ can be written in terms of a one-body, two body, three-body terms and so on. Considering Lennard-Jones potential, a simple intermolecular pair potential, describes two interacting particles repelling at very close distances and attracting at a moderate distance. Interaction approaches zero as the distance between the two approach inifinity. This potential is given by [93]:

$$V_{LJ}(r) = 4\epsilon[(\frac{\sigma}{r})^{12} - (\frac{\sigma}{r})^{6}] \tag{4.2}$$

where:

$$\epsilon = \text{potential well depth,}$$

$$r = \text{distance between the two particle,}$$

$$\sigma = \text{the diameter}$$

The r^{12} terms describes the repulsive potential while the $-r^6$ term contributes for the the attractive potential. If charge interactions is of interest and importance,

Coloumbs potential can be applied.

For intramolecular interactions, simplified bonded potentials include harmonic terms for bond stretching and angle bending, as well as torsion potentials that control rotations around bonds. Force fields specify the various constants (e.g., force constants for harmonic potentials) and often include cross-terms to better capture subtle interactions. Different force fields are optimized for specific applications [94, 95]. For example, AMBER is commonly used for proteins, biomolecules, and nucleic acids, whereas GROMOS has broader applications, including proteins, nucleic acids, glasses, and liquid crystals.

MD simulations are computationally intensive, typically limiting simulation times to the nanosecond or microsecond range [96, 97]. Key design considerations for an MD simulation include the time step, total simulation duration, and boundary conditions. The time step must be small enough to minimize discretization errors, typically set in the femtosecond range. The simulation box should be sufficiently large to prevent artifacts from boundary conditions. Various 3D geometries are used for the simulation space, with common shapes including cubic, hexagonal prism, and orthorhombic boxes [95]. As a simple example, the trajectory of BSA in water is presented in Appendix A.1.

Since PR65 is among the most frequently mutated subunits within PP2A, understanding the effects of point mutations on PP2A assembly mechanics is critical. Work by Anupam et al. investigates point mutations at hinge sites to probe the effects of these subtle changes [75]. The point mutated PR65 study combines MD simulation results with NOT analysis, where the end-to-end distance of mutated and wild-type proteins was averaged in a microensemble sense. The observed elongation or compaction of the protein correlated well with corner frequency and RMSD analysis from NOT measurements, providing valuable structural insights.

4.2 Results

Structural Impact of ATUX-8385 Binding: NOT Experimental Results

A home-built optical trapping setup and DNHs fabricated colloidally were used for the experiments as shown in Figure 4.3 . The trapping event was characterised as the change in transmission intensity due to dielectric loading and increase in noise

due to Brownian motion of the protein in the trap[98, 37, 44], see Figure 4.3c. A single jump in transmission level, as depicted in Figure 4.3c, typically represents an individual protein trapping event unless a protein exists naturally as a homo-oligomer. In the absence of other proteins, PR65 exists as a monomer and the trapping events observed were of single proteins. By contrast, multiple protein trapping events show up clearly in the signal, as has been reported in the literature for BSA and egg white protein[99, 6]. For our study, we focused on the difference between the trapped signal (transmission intensity picked up by the APD after the trapping event) of apo-PR65 in 5% DMSO and PR65 with ATUX-8385 in 5% DMSO. A total of 8 measurements were collected at 20 μM of ligand and a protein concentration of 10 μM.

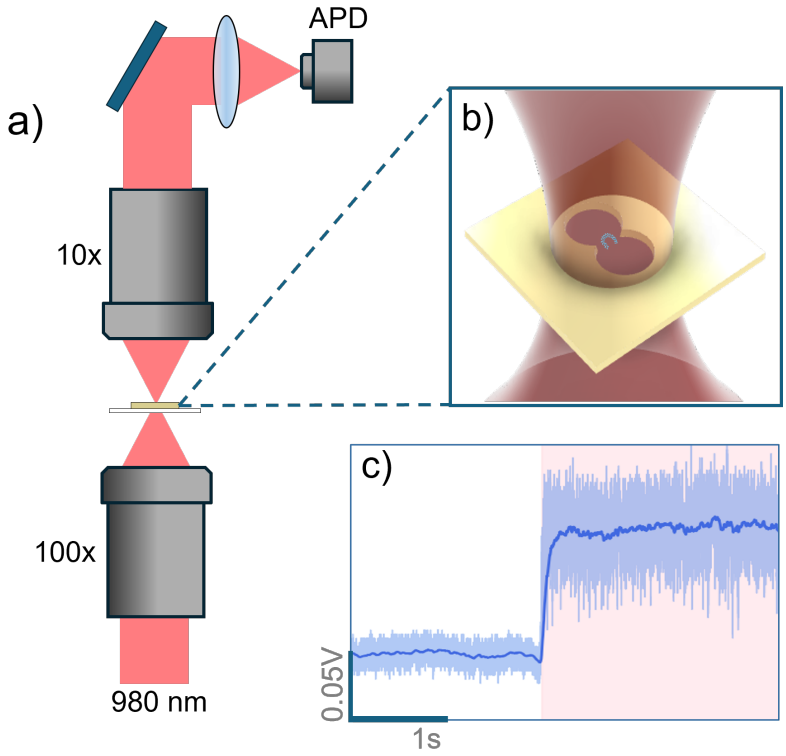

Figure 4.3: **Overview of NOTs trapping.** (a) Depiction of a simplified nanoaperture optical tweezer. (b) Cartoon representation, not to scale, of laser beam focused onto a DNH aperture with PR65 trapped between the DNH cusp. (c) Sample trapping signal of PR65 protein without SMAP, pink region shows when the protein has entered the trap.

A 100 sec segment of the trapped signal of PR65 and PR65 with ATUX-8385 from separate trapping events is shown in Figure 4.4. A 3 Hz low pass filter applied to the raw signal of PR65 renders a comparatively homogeneous signal when compared to the

signal of PR65 in the presence of ATUX-8385. In the presence of SMAP, the intensity of transmission fluctuates between two levels, showing a conformational change of the protein [100]. The intensity changes correlate with a change in the polarizability of the protein, hence, refractive index change of the protein[37, 101]. The molecular weight of PR65 is 65 kDa, which is reflected in its name. In contrast, ATUX-8385 has a molecular weight of approximately 500 Da, making it about two orders of magnitude smaller than PR65. In a previous work, the change in the standard deviation of the mean was linearly related to the protein size in the NOT system [44]. Based on this, we would expect a .7% change in standard deviation of the signal approximately with the additional mass, but in the experiment it approximately doubles (Figure 4.4b). Furthermore, our all-atom MD simulations of both the apo and ATUX-8385-bound PR65, presented in the following section, show a change in the conformation upon binding, which shifts the polarizability[101].

The probability density function (PDF) of the filtered signal is shown to the right of the time series signal. The 20 μM ATUX-8385 histogram was fit with two Gaussians for the bound and unbound states. The larger scattering signal voltage came from increased scattering (larger polarizability) and showed that binding of ATUX-8385 extends the protein. Extension of protein was also seen through the increase in the standard deviations of the Gaussian fits. Higher noise from the extended form of PR65 has been reported previously for point mutations [75]. While higher polarizability leads to a stiffer trap, it has a stronger effect on the scattering, as shown in past works[44].

To determine whether the extended form corresponded to the bound or unbound state, the experiment was repeated at a concentration of $5\mu M$ ATUX-8385 SMAP. At this reduced concentration, a lower frequency of the extended form was observed (see Figure A.4), suggesting that the higher transmission level corresponds to the bound state. Further support for this conclusion is provided by molecular simulation results discussed in the following section.

4.2.1 MD Simulation Results

Note: This section presents MD simulation results by Sema Zeynep Yilmaz, Anupam Banerjee, Satyaki Saha, Mert Gur and Ivet Bahar.

We performed molecular simulations to compare experimental and simulated structural impacts. Docking simulations for ATUX-8385 revealed a novel binding site. As

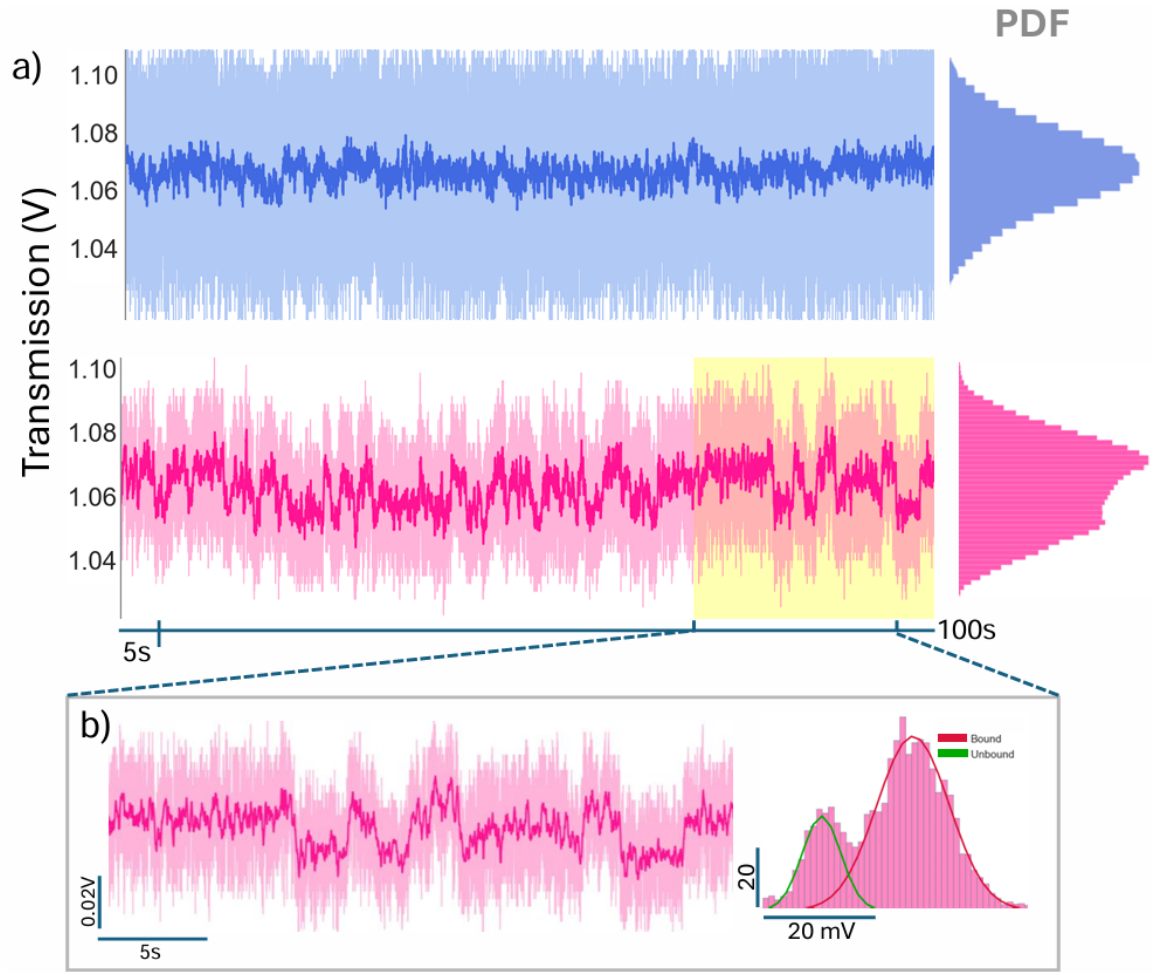

Figure 4.4: **Time series signal of the trapped PR65 with (pink) and without the presence (blue) of ATUX-8385 shows the interaction between protein PR65 and SMAP.** (a) The SMAP concentration used was $20\mu M$ while the protein concentration was fixed at $10\mu M$ Transmission signal from different DNH is shown. Lighter signal in the background is the raw signal while the solid lines are from the 3 Hz low pass filtered signal.PDF of the filtered signals are shown to the right of the time series signal. (b) PDF of the filtered signal fit with Gaussian functions further indicates the presence of a bound and unbound state. For the bound state, the Gaussian curve occupies an area(A_B) of 0.76 with a standard deviation(σ_B) of 0.004 V. Likewise, the unbound state Gaussian curve has parameters: A_U= 0.22, and σ_U= 0.002.

no structural data on the binding site/poses of the SMAP molecule ATUX-8385 on PR65 exist, we conducted a series of docking simulations on PR65 structure to determine a binding pose for ATUX-8385. Based on hydroxyl radical footprinting experiments, the K194–L198 region of PR65 was identified as a putative SMAP-binding region for a different tricyclic molecule, with K194, E197, and L198 as potential interaction sites[56]. Using this information, we performed guided docking simulations of ATUX-8385 onto PR65.

First, we used the Rosetta Ligand Docking Protocol 3[102] in the ROSIE server[103] to find the optimal binding pose of ATUX-8385 near E197. The compact conformation of PR65 (PDB: 6NTS, chain A) was used for docking simulations. The selected conformation binds to 4_i,5_i,5_o and 6_o, and has an interaction energy of -10.5 kcal/mol. All interaction energies are calculated using PRODIGY-LIG [104].

We then conducted additional docking simulations within 40Å radial distance from E197, so as to explore alternative docking poses and potential binding to PR65 residues near E101, where a related SMAP, DT-061, was reported to bind and stabilise the PP2A trimer [83]. Using AutoDock Vina 1.2.0 [105], docking simulations were carried out for both compact (PDB: 6NTS, chain A) and extended (PDB: 1B3U, chain A) forms of PR65. The selected conformations of ATUX-8385 with PR65 in the compact form and extended form led to interaction energies of -6.6 kcal/mol and -9.0 kcal/mol. Interestingly, the same binding site (near 4_i and 5_i) was shared between the compact and extended forms, while the extended form was significantly more favorable. We note that the coordinating residues D106 and R105 (among others) are adjacent to the DT-061 binding site in PP2A.

Since the conformation found using ROSIE was energetically more favorable, we proceeded with extensive MD simulations using this pose. MD simulations initiated from the compact PR65 structure showed that ATUX-8385 binding favored an extended conformation for PR65. Two sets of MD simulations were performed: one for apo PR65 and the other for the ATUX-8385 docked form of PR65. Each set was composed of three separate runs of 704 ns in length, totaling 4.224 μs of MD trajectory across both sets. ATUX-8385 remained in its docked position throughout all three runs, further validating this new binding site as a stable interaction point for ATUX-8385 on the PR65 monomer. ATUX-8385 binding impacted the structural preferences of PR65. While the apo PR65 runs fluctuated between compact and extended forms throughout the simulations, ATUX-8385 binding stabilised the extended PR65 form rapidly within 100 ns in two runs (Figure 4.5). Interestingly, in the other run, the

compact form was maintained for the first 500 ns before transitioning to an extended form. Collectively, these observations demonstrate that ATUX-8385 bound to the site formed by 4_i,5_i,5_o and 6_o stabilises the PR65 and favors the extended conformation. It should be noted that the fluctuations observed in the simulations are at a much faster timescale and do not correspond to the fluctuations seen in the experiment. The Boltzmann average binding affinity for this pose (Figure 4.5a), calculated over 2.112 μs of MD trajectory, was -9.6 kcal/mol.

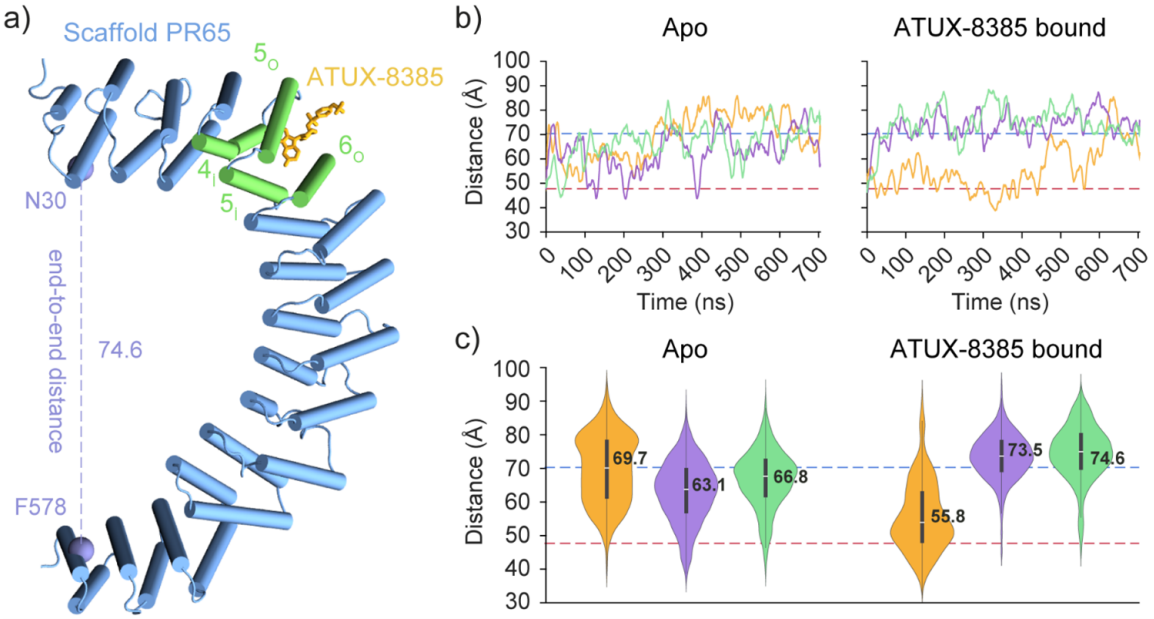

Figure 4.5: **Distribution of End-to-End Distances in Apo and SMAP-Bound PR65 from MD Simulations.**(a) Representative extended PR65 conformation stabilised by ATUX-8385, obtained from the third run. Distance between N30 and F578 α-carbons was used to define the structural form of PR65. (b) The end-to-end distance time evolution for runs 1-3 shown in orange, purple, and green. Dashed lines depict the end-to-end distances observed in the compact (PDB: 6NTS) and extended (PDB: 1B3U) structures of PR65. (c) Violin plots depicting the distribution of end-to-end distances for PR65 during the simulations under apo and ATUX-8385-bound states. For each distribution, mean values are indicated, and standard deviations are shown with thick bars.

Observation of Protein Binding Kinetics: NOTs Single Molecule Measurements

The 3 Hz low-pass filter was applied to the trapped signal of a single trapping event to track the mean movement of the transmission signal, filtering out higher-frequency noise while preserving the overall trend. The choice of filtering frequency can affect the results. Testing at 10 Hz showed that filtering was insufficient, allowing spurious noise artifacts to impact the data. At 1 Hz, however, the signal was overly smoothed and distorted. We selected 3 Hz as a compromise, balancing distortion and noise artifacts. This filtered signal was then segmented into approximately 30-second sections for easier processing, given the large file size. These sections were fit into step functions through a Hidden Markov Method (HMM) for identification of the two states (Figure 4.6a), see Methods for details. For each trapping event, ∼100 s of data was collected, segmented and analyzed. Cumulative distribution functions (CDFs) of the residence time in the bound and unbound state were fit with a single exponential (4.6) function to determine association (k_{on}) and dissociation rate (k_{off}) constants, Figure 4.6b. The good fit to a single exponential function suggests a 1:1 binding model between the protein and ligand. Association and dissociation cosntants of each single protein can be found in A. Across the measurements made (n=8), the signal showed a good consistency. Per 100 seconds, 111 ± 16 binding events occurred. The bound transmission intensity normalised to unbound transmission intensity was (101 ± 0.19)%. Table 1 summarizes the values for all measurements made at the $20\mu M$ ATUX-8385 SMAP concentration.

Table 4.1: Summary of interaction parameters between PR65 and SMAP ATUX-8385 found from single molecule NOT measurements(n=8).

$\tau_{off}(s)$	$\tau_{on}(s)$	$k_{off}\,(s^{-1})$	$k_{on}\,(s^{-1}\,\mu M^{-1})$	$\Delta G°$ (kcal/mol)	$K_D\,(\mu M)$
0.40 ± 0.06	0.37 ± 0.03	2.52 ± 0.42	0.19 ± 0.02	-6.72 ± 2.5	13.6 ± 2.5

Additional Characterisation of SMAP Binding to PR65

We used a range of biophysical techniques to confirm *in vitro* binding of SMAP ATUX-8385 to PR65 and to determine the binding affinity. The relatively low solubility of the small molecule (only soluble up to 100 μM in 10% DMSO, precluded the use of standard techniques such as Isothermal Titration Calorimetry (ITC), but we collected

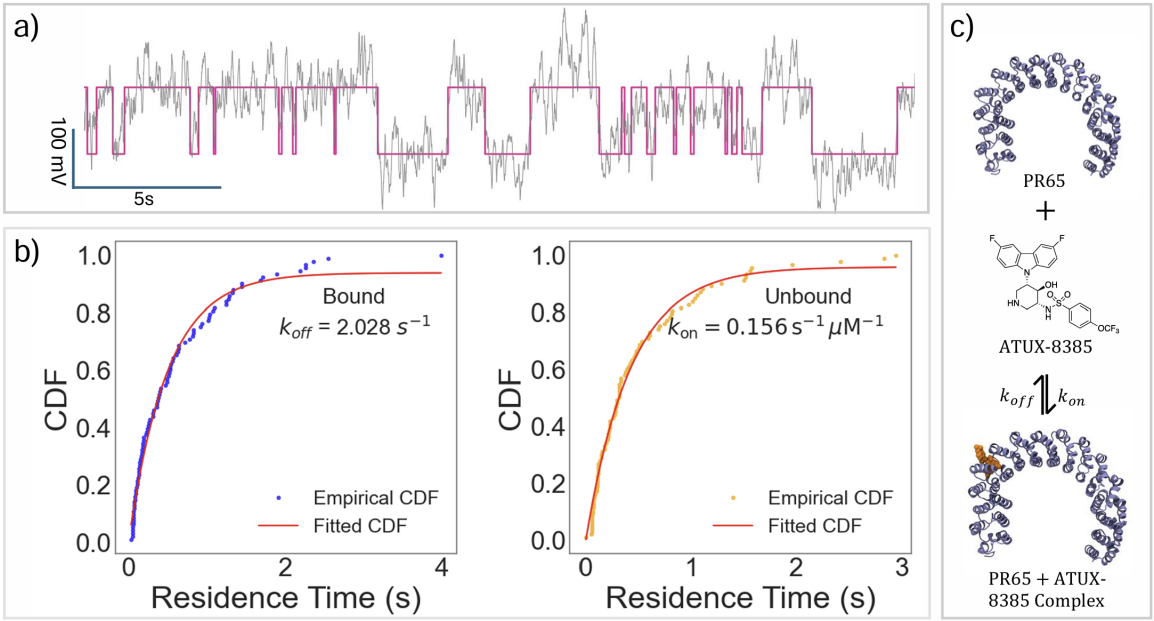

Figure 4.6: **Quantification of single molecule binding kinetics** (a) Step function fit to a 30s segment of trapped filtered signal. Higher scattering state corresponds to the protein-ligand complex. (b) CDFs of the residence time in bound/unbound states are fitted to a single exponential for the extraction of binding constants. A total of 94 events occurred in the 110 s analyzed. Coefficient of determination for bound and unbound CDF fitting are 0.9885 and 0.991 respectively. (c) Cartoon depiction of the 1:1 binding model

orthogonal data from three different biophysical methods to confirm that ATUX-8385 binds to PR65.

Nano Differential Scanning Fluorimetry (NanoDSF)

NanoDSF is a differential scanning fluorimetry technique used to assess changes in protein thermal stability in response to mutations, ligand binding, or buffer formulation changes. It measures the melting temperature (T_m), the point at which 50% of the protein has unfolded. This method relies on the intrinsic fluorescence of tyrosine and tryptophan residues, which become increasingly exposed as the protein denatures with rising temperature. When the small molecule binds to PR65, a shift in melting temperature is expected, as binding can either locally or globally stabilize or destabilize the protein. Thermal ramps were performed on 2 μM PR65 (10% DMSO) and the same concentration of PR65 in the presence of 100 μM ATUX-8385 (10% DMSO) to measure the melting temperature. In the presence of SMAP, a slight increase in the melting temperature was observed, indicating a stabilizing effect of the small molecule. With the control $T_{m,PR65} = 52.7 \pm 0.1°\text{C}$ shifting to $T_{m\text{PR65+ATUX}} = 53.5 \pm 0.1°\text{C}$. The slight change in melting temperature also suggests a weak micromolar binding affinity.

Nuclear Magnetic Resonance(NMR)

Nuclear Magnetic Resonance (NMR) is a technique used to investigate the local environment of specific nuclei within a molecule. It provides valuable information about the chemical structure and interactions of molecules. Common nuclei studied in NMR include ^{1}H, ^{13}C, ^{19}F, ^{31}P, and ^{29}Si. With the presence of Fluorine-19 in ATUX-8385, the interaction between PR65 and ATUX-8385 can be monitored through changes in chemical shift and relaxation rate. Upon addition of PR65, a small chemical shift was observed, suggesting that the electronic environment around the fluorine nucleus underwent only a minor change. Furthermore, the inverse relationship between relaxation rate and rotational correlation time further supports the binding of ATUX-8385 to PR65. Specifically, the relaxation rate decreased from $R2, ATUX = 6.93 \pm 0.05$ to $R_{2,ATUX+PR65} = 1.85 \pm 0.05$ upon the addition of PR65, confirming the formation of the ATUX-8385-PR65 complex (Figure 4.7c). The reduced relaxation rate indicates that the fluorine-19 nucleus is rotating more slowly due to its interaction with the larger PR65 protein, which restricts its movement.

Flourescence Polarisation (FP)

ATUX-8385 is a flourescent molecule with an exciation wavelength of 320± 10 nm and an emission wavelength between 340 to 550 nm. Maximum flourescence intensity is located at 370 nm. Exploiting the flourescent property of the small molecule, flourescence polarisation experiments were performed to obtain the ensemble binding affinity. This technique measures the change in the amount of polarised emisson by the flourophore. With small molecule unbound, rapid tumbling occurs and when excited by a polarised light source, its emission is larger unpolarised. When the small molecule forms complex with the protein, tumbling of the small molecule slows resulting in increased polarisied emission. Titration was performed with PR65 from a concentration of 1 μM to 80 μM to samples containing 2.5 μM, 5 μM, and 10 μM of ATUX-8385 (10% DMSO). The dissociation constant of 9.4 ± 1.4 μM was determined by fitting the polarisation data with a 1:1 binding curve.

4.2.2 Discussion

As PP2A holds a central role in many biological processes, there have been clinical investigations into PP2A directed therapeutics for preventing dysregulation in the enzyme. Here we explored a SMAP ATUX-8385 of tricyclic sulfonamide class that binds directly to the scaffold unit of PP2A, PR65, which has been shown to reactivate PP2A in a previous study [55]. We employed several approaches to gain novel insights into the effects of ATUX-8385 binding on the structure and dynamics of PR65, and the binding kinetics of PR65 and ATUX-8385.

Through docking simulations, a novel binding site, comprising residues at 4_i, 5_i, 5_o, and 6_o, for ATUX-8385 was identified. Subsequent extensive MD simulations confirmed the stability of this site and demonstrated that ATUX-8385 impacts the structural dynamics of PR65. In our simulations, ATUX-8385 binding was observed to favor the extended form. Specifically, binding of ATUX-8385 stabilised the extended form in two out of three simulations and the third run converged to an extended form towards the end of the simulation.

The docking of ATUX-8385 to the 4_i and 5_i shows promise, as indicated by its vicinity to known SMAP binding site. These novel binding sites differ from previously identified sites and suggests a potentially unique mechanism of action. These findings warrant further analysis in future work, including extensive MD simulations and experimental validation, to better understand the binding dynamics and func-

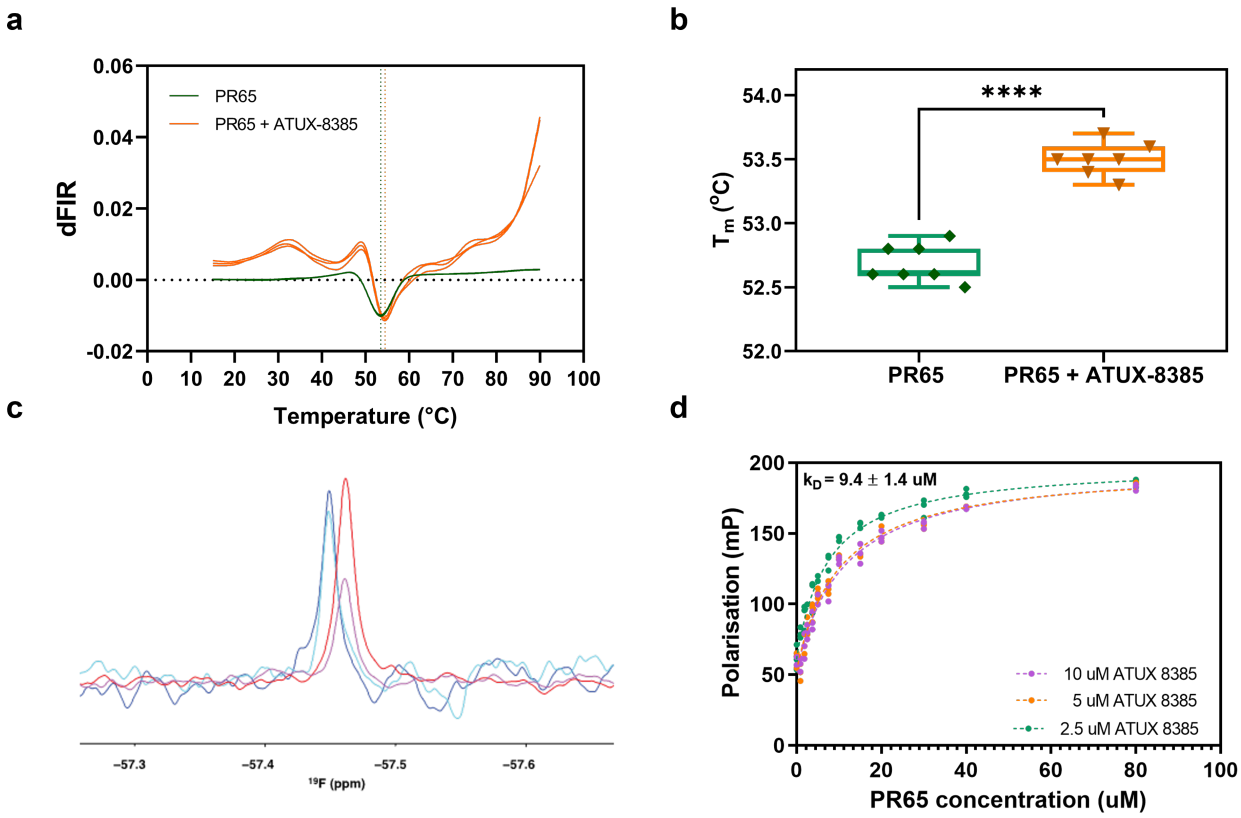

Figure 4.7: **(a) NanoDSF traces of the thermal denaturation of PR65 in the absence (green traces) and in the presence of ATUX-8385 (orange traces).** The data shown are the first derivative of the ratio of fluorescence intensities read at 350 nm and 330 nm (dFIR (350 nm/330 nm)). The global minimum corresponds to the melting temperature of the protein, T_m. A shift towards higher T_m values indicates an increase in stability induced upon SMAP binding. **(b) Extracted T_m values from the NanoDSF traces indicate an upwards shift in the presence of ATUX-8385($T_{m\mathbf{PR65}}$ = 52.7 ± 0.1 °C, $T_{m\mathbf{PR65+ATUX\text{-}8385}}$ = 53.5 ± 0.1 °C, N=7, p<0.001 via an unpaired t-test).** The NanoDSF experiments were performed with a Prometheus NanoDSF instrument (NanoTemper Technologies). 2 μM of PR65 in PBS, 2 mM DTT, was incubated either with 10% DMSO, or 100 μM ATUX-8385 in a final concentration of 10% DMSO, and thermal denaturation was performed from 20 °C to 90 °C with a 1°C/min rate. **(c)^{19}F NMR recorded at 298 K on ATUX-8385 indicates binding of the small molecule to PR65.** The NMR spectra show a drop in signal intensity upon binding of the small molecule, while the change in chemical shift is small as indicative of relatively weak binding. ^{19}F 1D CPMG experiments were performed for 100 μM ATUX-8385 in 10% DMSO (blue: transverse period 2 ms; cyan: transverse period 102 ms) or for 100 μM ATUX-8385 in 10% DMSO with 5 μM PR65 (red: transverse period 2 ms; magenta: transverse period 102 ms) on a Bruker Avance III 600 MHz (19F 564 MHz). **(d) Fluorescence polarisation experiments show ATUX-8385 binding on PR65 with a k_D in the low micromolar range.** Shown are the fluorescence polarisation values (mP) for 2.5 μM, 5 μM, and 10 μM ATUX-8385 upon PR65 titration, N=3. One-site fitting of the data (see methods for equation) gives K_D = 9.4 ± 1.4 μM.

tional implications of ATUX-8385 on PR65. Validation of the binding sites can be experimentally pursued by replicating this work with a point mutation near E197.

We produced two separate measurements of dissociation constants in this work: single molecule and ensemble. The dissociation constant found using the NOT approach comes from a single measurement on a single protein at a single SMAP concentration, while the ensemble measurement utilised the fluorescent property of ATUX-8385 to perform fluorescence polarisation experiments. The ensemble measurement required repeated measurements at different PR65 concentrations to establish the dissociation constant. The K_D obtained from both measurements are in good agreement with each other, and characterised ATUX-8385 as a molecule of weak affinity to bind to PR65. Using NOT, the observation of complex formation and dissociation in real time allows for determination of k_{on} and k_{off}. The change in the scattering signal with complex formation is consistent with the elongation of the protein upon binding, which provides biophysical data about the interaction. This stabilisation in the elongated form was also confirmed in MD simulations. Our past work quantified this elongation for various point mutations of PR65 [75].

Since the NOT technique depends on detecting light scattering changes induced by the activator upon binding, its applicability may be limited to binding pairs that produce a measurable scattering change, as not all interactions may result in detectable shifts. However, due to the same principle of the technique, the single-molecule binding assay is not restricted to the typical picomolar- or nanomolar range for techniques such as total internal reflection microscopy, smFRET. Fluorescence-based single molecule techniques are often confined to a low concentration barrier, as high concentration of fluorescent molecules results in an increase in background signal that in turn obscures binding events [7, 8].This is especially limiting as many biological processes are transient and have a dissociation constant in the micromolar range. Table 4.2 provides an overview of commonly used techniques for binding interaction anaylsis. Therefore, the NOT technique has an appropriate niche to study kinetics that can be observed on a timescale ranging from a microsecond to hundreds of seconds. For longer observation, a stable microscope setup is required to avoid drift over extended duration.

The NOT has an interesting feature of being able to tune the temperature by adjusting the trapping laser power [100, 39, 106, 46]. In the present work, we limited the power to achieve temperatures near physiological values; however, future studies can be undertaken to explore the impact of temperature on the binding kinetics. We

Table 4.2: **Comparison of binding interaction measurement techniques.** Surface Plasmon Resonance (SPR) and NOT do not have strict upper limits on ligand concentration, unlike fluorescence-based techniques. NOT distinguishes itself from other common binding kinetics methods by enabling the probing of structural dynamics during complex association and dissociation.

Technique	**Labelled?**	**Ligand Concentration**	**Structural Dynamics**	**Ensemble or Single Molecule**	**Surface Immobilization?**
SPR	Unlabelled	No upper limit specified	No	Ensemble	Yes
FRET	Labelled	pM–nM	No	Both	Yes
NOT	Unlabelled	No upper limit specified	Yes	Single Molecule	No, free-solution
TIRF	Labelled	pM-nM	No	Ensemble	No, free solution

did attempt a few temperature values by varying the laser power and saw insignificant variation in the dissociation constant over 4°C.

4.3 Methods

Protein Expression and Purification

GST-tagged PR65 was expressed in *E. coli* as described previously [107]. In brief, plasmid encoding PR65 was transformed into chemically competent C41 *E. coli* (Komander laboratory, MRC-LMB, Cambridge). Cultures were grown at 37°C in 2xYT medium containing ampicillin (50 μg/ml) until an OD600 of 0.6 to 0.8 was reached. Protein expression was induced with 500 μM isopropyl-β-d-thiogalactopyranoside (IPTG) (Generon) at 25°C overnight. Cells were harvested by centrifugation at 4000g for 10 min at 4°C before resuspending in lysis buffer [50 mM tris-HCl (pH 7.5), 500 mM NaCl, 2 mM dithiothreitol (DTT)] supplemented with EDTA-free protease inhibitor cocktail (Sigma-Aldrich) and deoxyribonuclease (DNase) I (Sigma-Aldrich). The cells were lysed by passing the suspension two to three times through an Emulsiflex-C5 (AVESTIN) at pressures of 10,000 to 15,000 psi. Soluble protein was separated from cell debris and other insoluble fractions by centrifugation at 35,000g for 35 min at 4°C. The soluble protein fraction was applied to glutathione resin

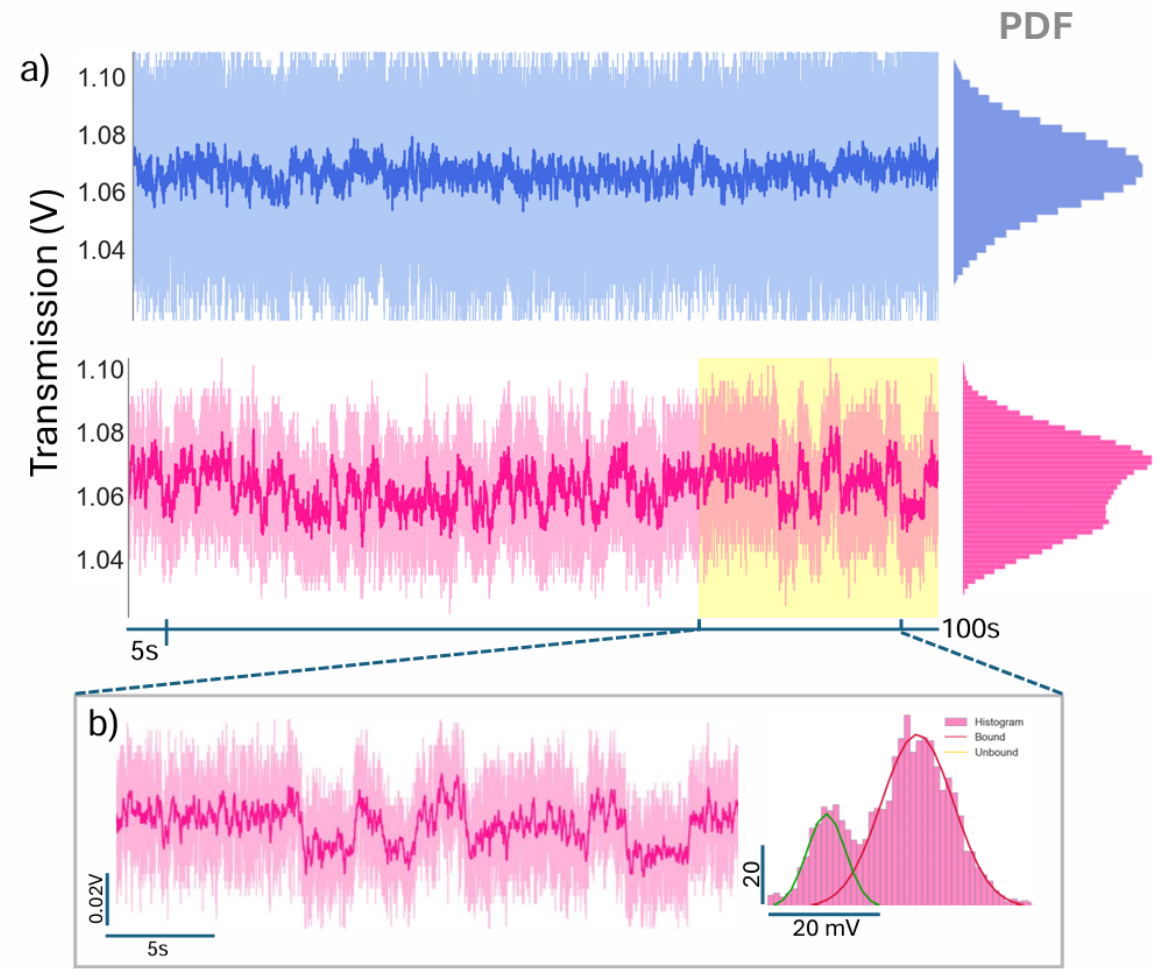

Figure 4.8: **Time series signal of the trapped PR65 with (pink) and without the presence (blue) of ATUX-8385 shows the interaction between protein PR65 and SMAP.** (a) The SMAP concentration used was $20\mu M$ while the protein concentration was fixed at $10\mu M$ Transmission signal from different DNH is shown. Lighter signal in the background is the raw signal while the solid lines are from the 3 Hz low pass filtered signal.PDF of the filtered signals are shown to the right of the time series signal. (b) PDF of the filtered signal fit with Gaussian functions further indicates the presence of a bound and unbound state. For the bound state, the Gaussian curve occupies an area(A_B) of 0.76 with a standard deviation(σ_B) of 0.004 V. Likewise, the unbound state Gaussian curve has parameters: A_U= 0.22, and σ_U= 0.002.

[Amintra Affinity, EGTA (0.5 g/liter), 2 mM DTT], the GST tag was cleaved with thrombin, and PR65 was eluted using a gravity column. After washing the column, the protein was subsequently eluted using a 20× column-volume salt gradient from

0 to 1 M NaCl. MonoQ fractions containing the protein were concentrated before application to a HiLoad 26/600 Superdex 200 pg (GE Healthcare) equilibrated in phosphate-buffered saline (pH 7.4) and 2 mM DTT. Samples were analyzed by SDS-PAGE (polyacrylamide gel electrophoresis) comparing the lysed, flowthrough, and eluted fractions. The identity of the protein was confirmed via MALDI mass spectrometry (Department of Chemistry, University of Cambridge).

DNH Nanoaperture Fabrication

The DNH fabrication follows our previous approaches [45, 108], as detailed in Chapter 3. Here, we outline specific variables in the fabrication process.

For this experiment, microscope slides were sectioned using a diamond scribe, sonicated in an ethanol bath for 10 minutes, rinsed with acetone and isopropyl alcohol, and blow-dried with nitrogen.To prepare the polystyrene sphere solution, 7.5 μL of ThermoFisher 300 nm PS was mixed into 1 mL of ethanol. Then, 10 μL of this PS-ethanol solution was deposited onto each slide in a zigzag pattern and left to dry overnight. The slides were plasma-etched using a Harrick PDC plasma cleaner for 135 seconds to fuse randomly distributed dimers and reduce cusp size, depending on etching time. A 7 nm titanium layer was sputtered onto the slides as an adhesion layer for gold, followed by a 70 nm gold layer. Finally, the PS spheres were removed by sonicating the slides for 7 minutes.

Sample Preparation for Trapping Experiments

The protein solutions comprised of phosphate-buffered saline solution with 0.01% (w/v) concentration, 2 mM of Dithiothreitol and 5% (v/v) Dimethylsulfoxide (DMSO). DMSO was used as a solvent for ATUX-8385. PR65 concentration was 10 μM while the ATUX-8385 concentration in solution was 20 μM. It is important to note that upon laser illumination, ohmic losses in the metal lead to local heating at the nanoaperture. Studies have shown that the temperature increase ranges between 0.64 K/mW to 4.25 K/mW [39, 106]. The temperature increase is experimentally shown to be dependent on the intensity of the incident laser, yet independent of aperture size, DNH cusp, and laser polarization[106]. The local temperature increase at the aperture was 0.64 K/mW [39, 6]. Unless otherwise stated, trapping experiments were conducted at an incident power that raised the temperature of the trapped protein to approximately 35 °C. A 50×2×0.13 mm coverslip was rinsed with acetone and

ethanol, then dried with nitrogen gas. A microwell was then formed by attaching an image spacer (Grace Bio-Laboratories GBL-654008-100EA) onto the coverslip. 9.5 μL of protein solution was then micro-pipetted into the microwell. The DNH slide, with the gold side facing the solution, was placed and sealed onto the image spacer.

Trapping Setup: Inverted Microscope

The trapping procedure follows Section 3.14. Notably, a 1.6 optical density filter (ODF) was used in all experimental runs to aid in DNH selection. By keeping the ODF fixed, DNHs were chosen as trapping sites by following the alignment procedure and verifying that the transmission voltage levels were acceptable and consistent with those of other DNHs used in the experiments.

NOT Data Acquisition and Analysis

Data was acquired at a sampling rate of 100 KHz using an Advantech USB-4711A data acquisition unit and analysed in Python and vbFRET. vbFRET was used for HMM fitting of the data for identifying state transitions. As the program was designed for single-molecule FRET data, input to the program must contain two columns of data corresponding to the donor and acceptor intensity [109]. The FRET efficiency is calculated as $I_{\text{Eff}} = \frac{I_A}{I_D+I_A}$. Given that we want to fit the trapping transmission data (I_T) as I_{Eff}, we must have the equivalence of $I_{\text{Eff}} = I_T$. This is achieved by setting $I_T = I_A$ and $I_D = 1 - I_A$. HMM fitting was applied with the setting of the number of maximum states as 2 and 20 fitting attempts.

After completing the HMM fitting, the fit was verified visually and refined using a custom Python script that corrects rapid state transitions in the time series data. The script identifies binary state values from the HMM fit and applies a 0.05-second duration threshold to detect potential spurious transitions likely caused by noise rather than actual state changes. For each transition detected within or below the threshold, the script compares the mean signal value during the brief state to the midpoint between the high and low states. If the mean value deviates by less than 10% from this midpoint, the transition is considered noise, and the state is reverted to the previous one. This correction process helps to remove spurious transitions, preserving both event duration and the integrity of the fit in the corrected time series. Refer to Figure SI-7 for the results of pre- and post-fitting improvements. Residence times are then collected after a quality check of the fitting.

Once all bound and unbound residence times are collected, we plot residence times as a CDF. This is then fit to the equation of $1-\exp\left(-\frac{x}{\tau}\right)$ using *scipy.optimize.curve_fit* , where τ is the time constant. Using equations given by the law of mass action, we calculated the binding rate constants as well as dissociation constant. We do not make the assumption of $[L]_{total} \approx [L]_{free}$ as this would introduce error to k_{on} and K_D as ligand depletion would remain unaccounted. Using time constants $\tau_{unbound}$ and τ_{bound} from the CDF fit, we use quadratic equation 4.7 to calculate for the free concentration of SMAP as well as τ_{on} and K_D.

The protein concentration $[P]$ and ligand concentration $[L]$ bind as:

$$[P] + [L] \underset{k_{\text{off}}}{\overset{k_{\text{on}}}{\rightleftharpoons}} [PL] \tag{4.3}$$

The on binding rate is given by:

$$k_{\text{on}} = \frac{1}{\tau_{\text{on}} \cdot [L]_{\text{free}}} \tag{4.4}$$

and the off binding rate is given by:

$$k_{\text{off}} = \frac{1}{\tau_{\text{off}}} \tag{4.5}$$

From these, the dissociation constant can be determined as:

$$K_D = \frac{\tau_{\text{on}} \cdot [L]_{free}}{\tau_{\text{off}}} = \frac{[P][L]}{[PL]} = \tau^*([L]_t - [PL]) = \frac{([P]_t - [PL])([L]_t - [PL])}{[PL]} \tag{4.6}$$

where we have exploited the relation:

$$([PL]^2 + \tau^*[PL]^2) - [PL] \cdot ([P]_t + [L]_t + \tau^*[L]_t) + [P]_t \cdot [L]_t = 0 \tag{4.7}$$

The Gibbs free energy of association is calculated using this equation.

$$\Delta G^\circ \ = RT \ln K_{\text{D}} \tag{4.8}$$

Docking Simulations

ATUX-8385 was docked to PR65 using ROSIE[103] and AutoDock Vina [110]. Before initiating the docking simulations using AutoDock Vina, hydrogens were added

to both protein and ligand, and the structures were saved in the PDBQT file format utilizing AutoDock Tools (ADT) 1.5.6 [105]. Subsequently, partial charges for all ligands were calculated using the Gasteiger method within ADT. The added hydrogens in ligand were manually inspected. Following this verification, a 3-dimensional grid box was constructed with varying sizes ranging from 20 Åto 40 Å, maintaining a grid spacing of 1 Å. The center of the initial grid box was set based on the ATUX-8385 docked structure obtained from ROSIE.

System preparation for MD simulations

The structure of monomeric PR65 was derived from the DT-061 bound trimeric PP2A structure (PDB: 6NTS[83]) with a resolution of 3.63 Å, in which PR65 adopts a compact form. The coordinates for ATUX-8385 docked at 4_i,5_i,5_o, and 6_o were obtained from our docking simulations. Each of apo and ATUX-8385 bound PR65 structures was solvated in a water box containing explicit TIP3P[111] water molecules, with a box size 144 Åin all directions. To neutralize the system and set the ion concentration to 150 mM NaCl, Na+ and Cl- ions were added. The system size was approximately 286,900 atoms. All system preparation steps were conducted using VMD[112].

Details of MD simulations

MD simulations were conducted using the NAMD 3[113] software, employing the CHARMM36 all-atom additive protein force field[114]. A 2 fs time step was used throughout the simulations. Temperature was maintained at 310 K via Langevin dynamics, utilizing a damping coefficient of 1 ps-1, and pressure was held at 1 atm using the Langevin Nosé-Hoover method with an oscillation period of 100 fs and a damping time scale of 50 fs. Van der Waals interactions were calculated with a cut-off distance of 12 Å, while the particle-mesh Ewald method was applied for long-range electrostatic interactions. Two rounds of system minimization and equilibration were executed before each production run. Initially, the protein structure was kept fixed and the system was to 10,000 minimization steps, followed by a 1 ns of equilibration. This first round of minimization-equilibration was designed to equilibrate the solvent around the protein. Subsequently, we performed a second round of minimization-equilibration, in which the system underwent an additional 10,000-step minimization without any restrictions on protein structure and dynamics, followed by a 2 ns of equilibration, applying harmonic constraints (k=1 kcal/mol/$Å^2$) only on the Cα atoms.

After these preparatory simulations, we removed all constraints and initiated the production runs. Apo PR65 simulations were extended to a total duration of 704 ns from our previous study[75], where each simulation was 654 ns in length. In contrast, all system preparation and production runs for ATUX-8385 bound PR65 were entirely performed in this study.

Nano-differential Scanning Calorimetry (nanoDSF)

PR65 samples (2 μM) in PBS, 2 mM DTT were mixed with ATUX-8385 to a final concentration of 100 μM, 10% DMSO and in a total volume of 20 μL. The mixtures were allowed to equilibrate at room temperature for 10 minutes. High-sensitivity capillaries (NanoTemper) were filled with the equilibrated PR65-SMAP mixtures using capillary forces, ensuring no air bubbles were present. The capillaries were loaded into the Prometheus NT.48, and a thermal ramp from 20°C to 90°C at a rate of 1°C per minute was applied. Intrinsic tryptophan and tyrosine fluorescence at 330 nm and 350 nm was continuously monitored. The melting temperature (T_m) was determined from the first derivative of the fluorescence ratio (I350/I330) with respect to temperature. The T_m corresponds to the inflection point of the melting curve.

Fluorescence Polarisation (FP)

A fixed concentration of ATUX-8385 (2.5 μM, 5 μM, and 10 μM) was mixed with varying concentrations of the protein (0 to 80 μM) in a total volume of 20 μL in each well of a 384-well microplate (Greiner), to a final DMSO concentration of 10%. The plate was incubated at 40°C for 30 minutes to ensure binding equilibrium. Fluorescence polarisation was measured at 40°C using an excitation wavelength of 295 $\pm$ 10 nm and an emission wavelength of 360 $\pm$ 20 nm, on a CLARIOStar (BMG Labtech) measuring the light in parallel and perpendicular planes relative to the excitation plane. Wells containing only ATUX-8385 (without PR65) and wells containing only PR65 were used as controls to determine background fluorescence and polarisation values. Fluorescence polarisation (P) was calculated using the equation:

$$P = \frac{I_{\parallel} - I_{\perp}}{I_{\parallel} + I_{\perp}} \tag{4.9}$$

where $I_{\parallel}$ and $I_{\perp}$ are the intensities of fluorescence parallel and perpendicular to the excitation plane, respectively. Non-linear regression analysis was performed using a

one-site binding model to fit the data and determine the dissociation constant K_D, using the following equation:

$$P = \frac{P_{\max} \cdot C_{\mathrm{PR65}}}{k_D + C_{\mathrm{PR65}}} \tag{4.10}$$

where P is the polarisation, $P_{\max}$ is the maximum polarisation at the plateau, C_{PR65} is the concentration of PR65 (μM) and K_D is the equilibrium dissociation constant.

19F Nuclear Magnetic Resonance (NMR)

NMR samples containing 5% D_2O were prepared with ATUX-8385 added to a final concentration of 100 μM in 10% DMSO. NMR spectra were recorded at 298 K on a 600 MHz (^1H) Bruker Avance III spectrometer equipped with a 5 mm QCI HFCN/z cryoprobe (^{19}F 564 MHz) (Department of Biochemistry, University of Cambridge). 1D ^{19}F NMR data were obtained with 256 scans for ATUX-8385 in the presence of PR65 and 128 scans without the protein and recorded as 1D CPMG experiments (the separation between neighbouring 180° pulses was 100 μs).To assess binding of ATUX-8385 the intensities of pairwise experiments recorded with 2 ms and 102 ms transverse delay time were compared and the intensity ratios were converted into transverse relaxation rate R_2 values.

4.4 Concluding Remarks

In this study, we explored a SMAP ATUX-8385 of tricyclic sulfonamide class that binds to PR65 and has been shown to reactivate PP2A in a previous study aimed at cancer therapeutics [55]. We used NOT, a single molecule technique, to determine the dissociation constant of 13.6 ± 2.5 μM, agreeing with fluorescence anisotropy measurements while not requiring a titration: the experiment was performed on a single protein molecule and was highly repeatable. The NOT approach showed increased light scattering upon binding, which is consistent with an extension of the protein upon binding, as found in MD simulations. The MD simulations also elucidated the binding site. Therefore, the NOT, combined with all-atom MD simulations, provided information on the conformational changes taking place upon SMAP binding. Such mechanistic data are useful for clinical certification of SMAPs.

Label-free single particle analysis techniques are changing the landscape of biomolecule investigations, with recent successful commercialization of iScat[115, 116], nanopores[117,

118] and tethering-based force-measurement [119, 120] techniques. The NOT approach allows for valuable data extraction on small molecule binding for drug discovery applications, not only quantifying the binding affinity, but also giving insight into the impact of binding on the structure of the protein. It also has the advantage of working on a single molecule, not requiring additional steps like titrations or labelling, using less sample and allowing for tuning the local temperature at the protein by changing the laser power. Therefore, we believe that there is potential for this technique to be widely adopted in drug discovery and other research areas.

Chapter 5

Other Works

This chapter highlights two other projects that I worked on during my program. As a summary, this chapter will be comprised of the following subsections:

- Binding study of point mutated PR65 and ATUX-8385: This is an extension of the study presented in chapter 4 where the wild type PR65 protein is swapped out with a point mutated form of itself.
- Rapid and Cost-Effective Fabrication of a Nanoscale Optical Trapping Microfluidic Chip

5.1 Y168V Point Mutation

As previously discussed, the scaffold protein's ability to fluctuate between closed and open conformations is crucial for the accessibility of the substrate-binding interface. Disruptions in PR65's ability to sample closed or extended conformations can lead to the failure of PP2A assembly. Given the high frequency of mutations in PR65, the effects of point mutations at hinge sites were investigated using MD simulations and NOT [75]. Six different PR65 point mutations were analyzed for their conformational sampling and ability to transition between open and closed states.

Here, we focus specifically on the Y168V mutation, where a tyrosine residue at position 168 is replaced by valine (Figure 5.1). Based on three MD simulation runs, this mutation notably affected the structure's ability to uniformly sample conformational space. Individual runs gravitated toward different conformations. However, the native property of the wild-type protein to fluctuate between closed and open

states on the nanosecond timescale remained mainly unaffected by this specific point mutation.

Figure 5.1: **PR65 protein with mutation at site 168, Valine replacement of Tyrosine residue.** Figure adapted from reference [75].

Expanding on the investigation of point mutation, binding experiments between ATUX-8385 and Y168V point mutated PR65 protein were performed. Below we present the preliminary results of the binding interaction study.

5.1.1 Results

Similar to Chapter 4, small molecule–protein interactions are investigated by comparing the trapping signals of the Y168V mutant in the presence and absence of ATUX-8385. The time traces clearly show that, in the presence of the small molecule, transmission levels fluctuate between two distinct states (Figure 5.2). Fitting the time trace further reveals transitions between these states.

To gain deeper insight into the structural dynamics of binding, MD simulations and experiments with lower ligand concentrations should be conducted. Without complementary studies, it remains unclear whether the complex consistently adopts a more extended or compact conformation upon binding. Nevertheless, the observed transient behavior suggests that this specific point mutation likely does not negatively impact the binding region.

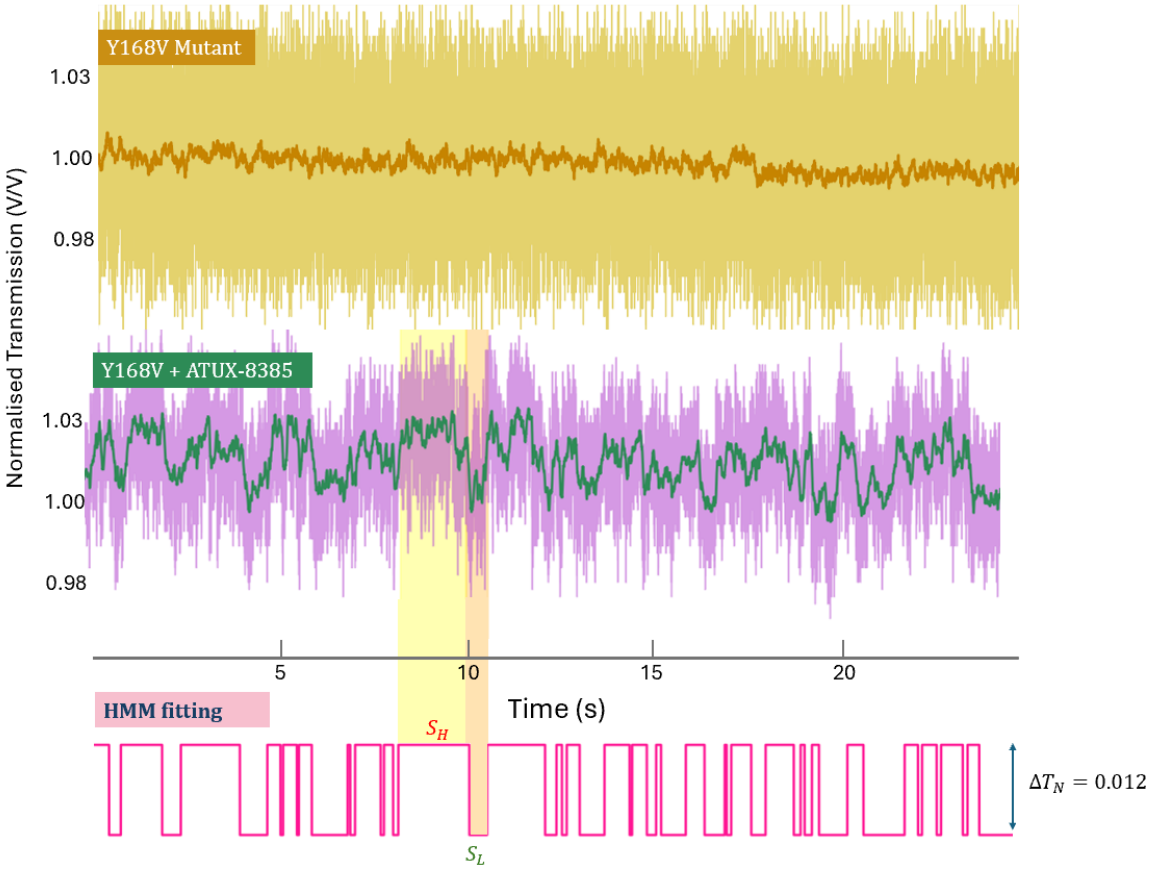

Figure 5.2: **Trapped time traces of normalized transmission (V/V) for the Y168V mutant protein in the presence and absence of ATUX-8385.** Both time series signals represent the transmission *after* the protein has been trapped inside the nanoaperture. **Y168V mutant:** 10 μM Y168V protein with 5% DMSO. In the absence of ATUX-8385, the low-pass filtered signal (brown) remains steady with minimal variations, indicating that the protein predominantly samples a single conformational state. **Y168V + ATUX-8385:** A solution of 20 μM ATUX-8385 dissolved in DMSO is introduced into a 10 μM Y168V protein solution(5% total DMSO). The trapped signal exhibits clear transitions between two distinct states, suggesting conformational changes upon ligand binding. **HMM fitting:** A hidden Markov model (HMM) is applied to the time trace, revealing two well-defined states: S_H, characterized by higher transmission levels, and S_L, corresponding to lower transmission values.

5.1.2 Conclusion

We present a preliminary interaction study between ATUX-8385 and the Y168V point-mutated PR65 protein. The apo Y168V signal remains stable, showing no signatures of conformational changes. However, in the presence of ATUX-8385, the protein exhibits fluctuations between extended and compact conformations. This observation warrants further investigation into the differences in binding kinetics between the wild-type and point-mutated protein.

5.2 Rapid and Cost-Effective Fabrication of a Nanoscale Optical Trapping Microfluidic Chip

To systematically study the effects of biomolecular interactions and environmental changes, integrating a fluidic system into the existing NOT setup is highly desirable. Several studies have demonstrated the use of fluidic-integrated NOT systems. For instance, the transition between the iron-loaded and apo-ferritin states of a single ferritin protein was observed for the first time using a resin-based flow cell [5]. Additionally, BSA and anti-BSA interactions were studied using NOT with a PDMS-based flow cell [121].

In this study, we designed and fabricated a microfluidic chip specifically for nanoscale optical trapping. This microfluidic chip is unique in that it can be integrated into any optical tweezer setup without modifications to the existing system. The fabrication process combines multiple techniques, including colloidal lithography for DNH fabrication and patterned cutting of Parafilm to create the fluidic channel [122].

Using our rapid and cost-effective microfluidic chip, we perform a test case of trapping Cytochrome C and observe the impact of flow on signal quality.

5.2.1 Methods

The fabrication steps of the flow cell can be summarized as follow:

1. **Drill two holes** (inlet and outlet) on opposite sides of a microscope slide using a $\sim$1 mm radius diamond drill bit.

2. **Clean the slide** with acetone and ethanol, then sonicate it in an ethanol bath for 10 minutes. Rinse thoroughly and let it dry.

3. **Deposit polystyrene beads** (in solution form) onto the slide and allow them to dry overnight.
4. **Plasma etch the slide** to achieve the desired cusp size.
5. **Sputter the slide with gold.**
6. **Remove the beads** by sonicating the slide in ethanol for 7 minutes.
7. **Fabricate the fluidic channel** by cutting Parafilm into a pre-designed pattern using a commercially available cutting machine.
8. **Thermally bond** the coverslip, Parafilm, and DNH slide at 55°C for 15 minutes, applying a 2.5 kg weight onto the sample.
9. **Attach the fluidic interfaces** (Fluidic 360 #10000700) to the holes in the DNH slide:
   (a) Sanitize a thin wire and set it aside.
   (b) Carefully remove one side of the adhesive ring (#10000717).
   (c) Thread the fluidic interface onto the wire, followed by the sticky side of the adhesive ring.
   (d) Adhere the ring to the interface.
   (e) Remove the other side of the adhesive ring, thread it through the inlet hole, and slide the fluidic interface down to the glass slide. Press firmly to secure the interface.
   (f) Apply nail polish around the inlet port and let it dry for ∼15 minutes.
   (g) Carefully apply Krazy Glue to fully seal the connection.
   (h) Repeat the process for the outlet.
   (i) Allow the assembly to dry overnight.

After allowing the chip to dry overnight, it should be tested for leaks before use. To do this, fill a syringe with distilled water and attach tubing to the inlet. Connect the tubing from the outlet to a waste collection Eppendorf tube. Set the flow rate to approximately 20–1 µL/min and let it run for 1 hour. The flow rate should not exceed 40 µL/min, as excessive pressure has consistently caused chip failure. At 40 µL/min, the chip may function as intended for a few minutes before failing. However,

at the recommended flow rate, the coverslip, Parafilm, and gold-coated slide should withstand the pressure. If a leak is detected at the seal, allow the chip to dry and reseal it using Krazy Glue and nail polish. If the leak originates from the Parafilm seal, the fabrication process must be repeated. To reuse the fluidic interfaces, soak the chip in an ethanol bath, carefully peel away the glue, and detach the interface for future use.

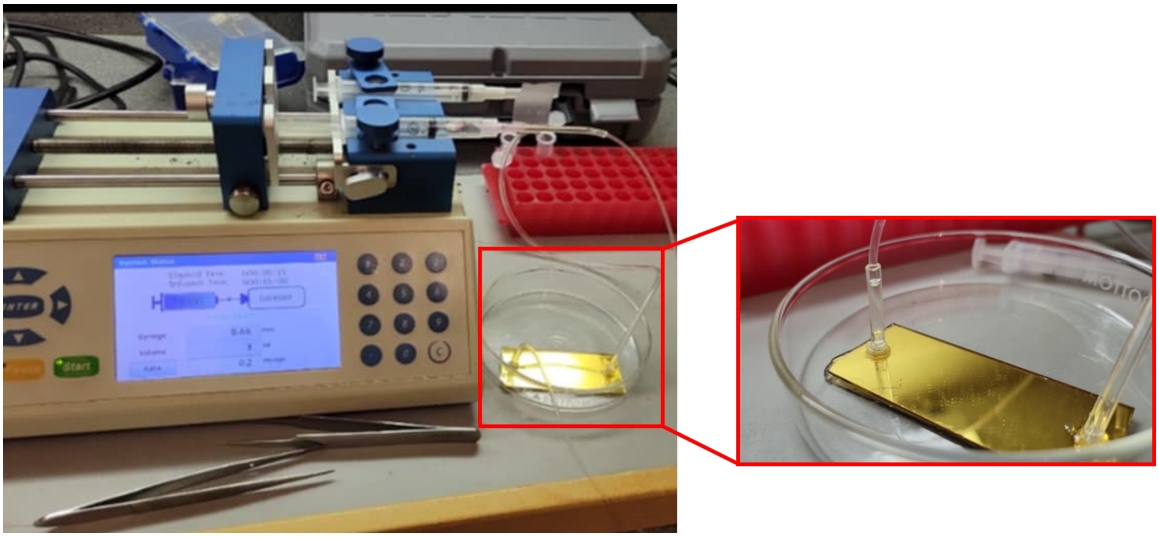

Figure 5.3: **Simple fluidic chip test bench** Chips are subjected to around 1 hour testing before use. If no leaks are observed, the chip is flushed with 2 cycles of ethanol wash and followed up with a wash of distilled water.

5.2.2 Results

To perform trapping with the fluidic chip, the assembled chip with tubing in place was positioned onto the sample stage (Figure 5.4a). Due to equipment limitations, such as the absence of a MUX distributor, microfluidic flow swtich valve, for sequential sample switching, the syringe pump filled with PBS buffer was directly connected to the inlet, while the outlet fluidic interface had a short tubing (≈ 2 cm) attached. PBS buffer was pushed through the setup until it reached the top of the outlet tubing.

The standard trapping procedure, as described in Chapter 3, was then followed. When the system was properly flushed and cleaned, no particles were trapped, and the APD signal remained stable. Once this was confirmed, the laser was turned off, and 20 μL of Cytochrome C was carefully pipetted into the outlet tubing. The pump

was set to pull at a flow rate of 10 μL/min and was stopped once the liquid reached the bottom of the outlet tubing. Trapping was then resumed following the standard procedure.

Cytochrome C was successfully trapped using the fluidic chip. The entry of Cytochrome C into the trapping site is evident from the change in transmission and noise level, transitioning from point (a) to point (b) in the top figure of Fig. 5.5. To evaluate the ability of the optical tweezer to hold on to the protein under a flow rate of 5 μL/min, the pump was turned on to push the buffer toward the outlet.

In the time series signal, significant drift becomes apparent around the 20-second mark. This drift may have originated from the pump motor, which was positioned near the tweezer on the same optical table. Additionally, the fluidic chip was not securely affixed to the sample stage, potentially allowing micromovements.

To assess the impact of this drift on the corner frequency, which is related to trapping stiffness, the highlighted portion of the time series signal is divided into seven equal segments. As per the standard method for NOT analysis, a Lorentzian function is fitted to the square modulus of the Fourier-transformed time series signal to determine the corner frequency. The corner frequency remains stable up to the 27–32 s time interval (Fig. 5.5, bottom right). However, a significant reduction in stiffness is observed, corresponding to the steepened slope in transmission drift.

Conclusion

This section provides an overview of the fabrication of a NOT fluidic chip and a trapping test case using Cytochrome C. The primary focus has been on the fabrication of the flow cell, while further work is needed to optimize the fluidic system itself. Basic recommendations for future improvements include incorporating a MUX distributor to enable efficient and reliable fluid switching at the inlet. With this modification, the outlet would function as a waste stream. Integrating a fluidic chip with a NOT system would allow for the observation of biomolecular interactions or conformational changes before and after perturbations.

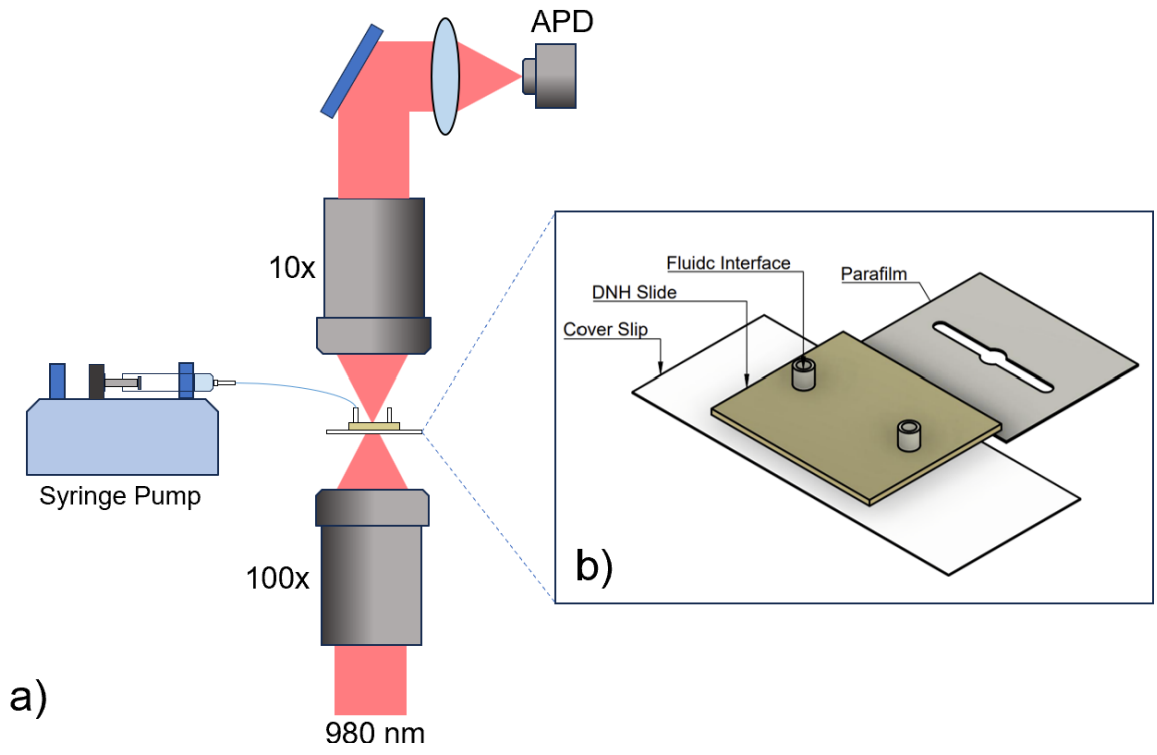

Figure 5.4: **Simple fluidic chip integration with the NOT setup.** **(a)** The fluidic chip is positioned on the NOT sample holder stage. A syringe pump is connected to the chip via approximately 20 cm of tubing. **(b)** Exploded view of the fluidic chip, which consists of a three-layer structure: a cover slip, patterned Parafilm, and a DNH slide (from top to bottom).

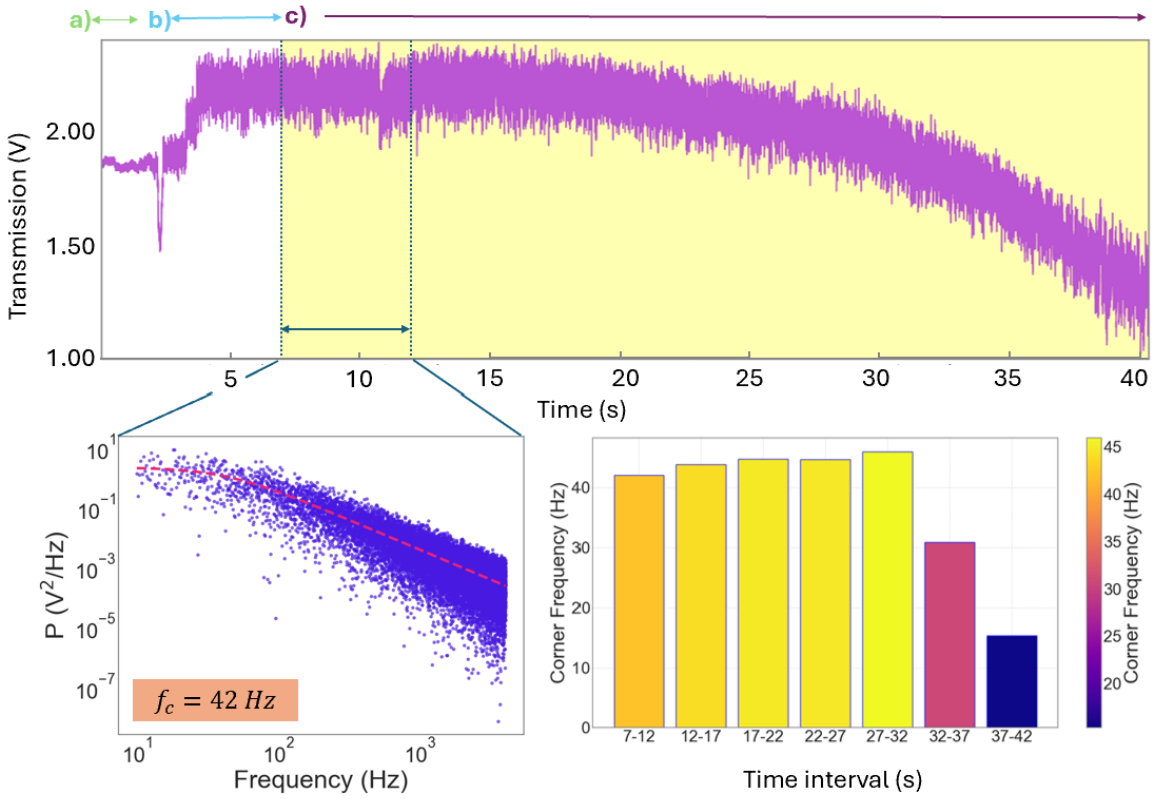

Figure 5.5: **Cytochrome C Trap Signal. Top**: The trace begins after Cytochrome C is introduced into the channel. (a) The double nanohole (DNH) is empty, and the laser is on. (b) Cytochrome C enters the trapping site, inducing a change in transmission levels. (c) The pump is activated, generating a flow rate of 5 μL/min toward the outlet, while the protein remains trapped. **Bottom left**: Power spectral density (PSD) of the signal calculated from the 7–12 second segment of the time series. A Lorentzian function (pink dotted line) is fitted to extract the corner frequency, f_c, of 42 Hz. **Bottom right**: A highlighted segment of the time series is divided into seven consecutive 5-second intervals to reveal changes in the corner frequency associated with the observed drift.

Chapter 6

Conclusions

In this thesis, we explore the development of NOTs, where the seemingly simple addition of a nanoaperture to a single-beam optical tweezer has unlocked the ability to manipulate light at the nanoscale. This achievement provides a unique window into the mechanics of life. Proteins play central roles in nearly every stage of the cellular lifecycle, and with more than half of human proteins estimated to be less than 4 nm in radius, it is crucial to understand their detailed mechanisms for both fundamental science and medical advancements.

The processes of phosphorylation and dephosphorylation, mediated by kinases and phosphatases, respectively, regulate key biological functions such as cellular signaling, homeostasis, and cell cycle progression. Disruptions in these tightly regulated processes are linked to chronic illnesses, including cancer, neurodegenerative diseases, and cardiovascular disorders. In particular, we discuss the dysregulation of PP2A —a phosphatase that, despite comprising 1% of total cellular protein, is highly susceptible to mutations. These mutations contribute to disease progression, with early research efforts showing that reactivation of PP2A using tricyclic small molecules can significantly reduce cancer cell proliferation, warranting further investigation.

In Chapter 4, we present a collaborative study on ATUX-8385 and wild-type PR65, a regulatory subunit of PP2A. NOT experiments provide insight into structural changes induced upon complex formation. Upon binding, the protein adopts a more extended conformation, leading to an increase in transmission. At this stage, the observed structural effects remain qualitative, as the precise relationship between transmission changes and protein-specific elongation requires further theoretical and simulation-based analysis. Additionally, dissociation constants obtained from single-molecule NOT experiments and ensemble measurements are in good agreement, in-

dicating that ATUX-8385 binds weakly to PR65 with a micromolar dissociation constant. Preliminary studies of ATUX-8385 binding to a Y168V point mutant of PR65 suggest that complex formation and dissociation still occur.

Following this, efforts toward the fabrication of a Parafilm-based fluidic chip are discussed. A natural progression of interaction studies would be the integration of a fluidic system, enabling controlled introduction of various stressors or binding agents to a single nanoaperture-trapped protein, while maintaining strict control over experimental variables. The foundation of an economical, low-tech flow cell with integrated nanoapertures has been established. Future work should focus on quantitative stress testing, as well as incorporating a MUX distributor, flow rate monitoring, and other enhancements to improve reliability and precision.

A comprehensive binding interaction study between PR65 wild type and its point mutated form could help elucidate how specific point mutations affect small-molecule binding or aid in experimentally pinpointing binding regions. Furthering our understanding of the mechanisms of the scaffold unit could advance drug development by enabling more effective binding and potentially making drugs less susceptible to protein mutations.

Appendix A

Additional Information

A.1 Molecular Dynamics : BSA in Water

Using GROMACS, an open source package for performing molecular dynamics simulation, a short 0.5 ns simulation run of BSA is completed. It should be noted that the simulation time is set due to CPU limitations. 1 ns of simulation time translates to 36 hours of computing time.

The main motivation of this study is to further investigate the thermal unfolding and folding of BSA, as previously reported by Peters et al. The crystal structure of BSA (PDB: 3V03) was used as the starting model for MD simulations (Figure A.1). The protein was placed at the center of a cubic simulation box filled with water as the solvent. Since BSA has a net charge of -32e, counterions were added to neutralize the system. Additional ions were included to better mimic physiological conditions.

To prevent steric clashes and high-energy, unrealistic conformations, energy minimization was performed. Energy minimization optimizes atomic positions to reduce the overall potential energy and eliminate unfavorable interactions. The simulation temperature was set to 300 K. Prior to the full MD run, equilibration steps were carried out to stabilize the system in terms of temperature, pressure, and density (A.2).

The time series RMSD (right panel of Figure A.3) shows a steady increase throughout the simulation. By the end of the run, the RMSD of the protein rises above 0.20 nm, suggesting that the structure may not be stable. In terms of the radius of gyration, a fluctuation of 0.05 Å is observed during the run. A longer simulation is needed to determine whether this fluctuation is typical for BSA or if the protein is undergoing

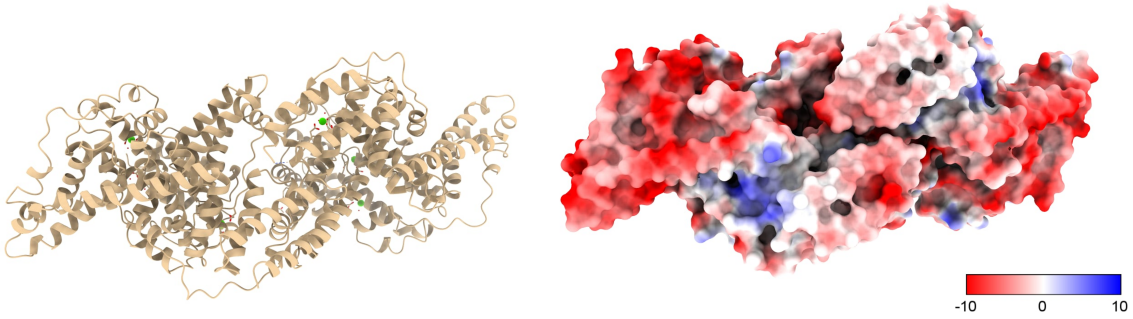

Figure A.1: **Bovine Serum Albumin (PDB: 3V03) Model.** The ribbon representation of BSA is shown alongside its electrostatic surface view. The model was rendered using Chimera software. Molecular graphics and analyses performed with UCSF Chimera, developed by the Resource for Biocomputing, Visualization, and Informatics at the University of California, San Francisco, with support from NIH P41-GM103311.

an unfolding process. By altering the system temperature, thermal unfolding/folding of BSA can be studied using MD simulation to complement experimental results.

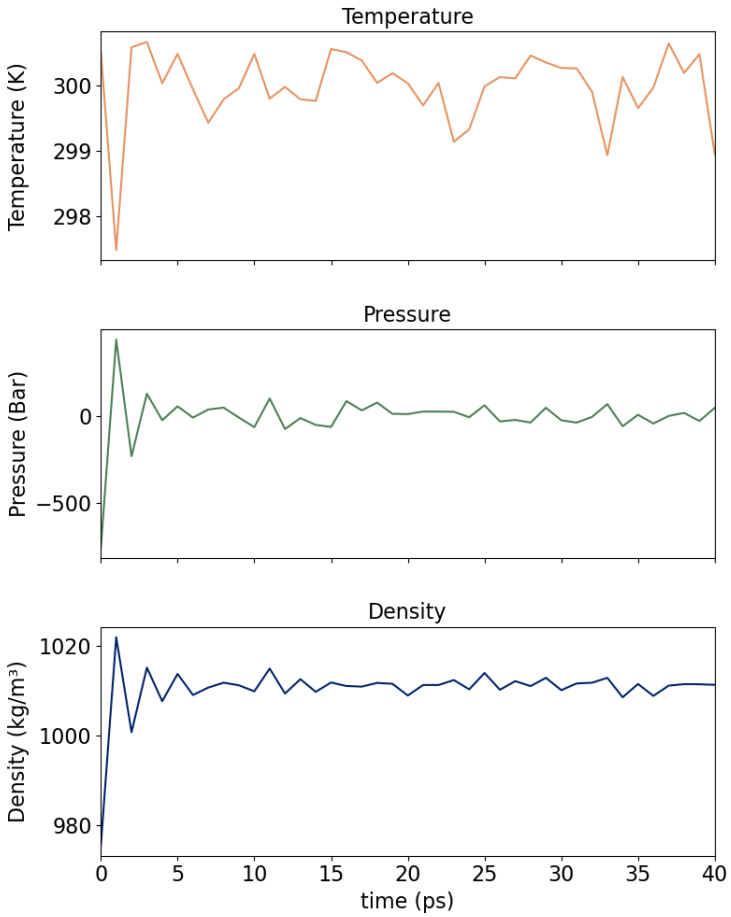

Figure A.2: **Equilibration of system with single BSA protein in water** Temperature(orange) quickly reaches the target temperature of 300K and averages at 299.5 $°C$. Although the reference pressure of 1 bar drops quite quickly, the pressure(green) becomes relatively steady throughout the remaining equlibriation time. Density(blue) equilibrates close to the expected value for the solvent (1000 kg/m^3)

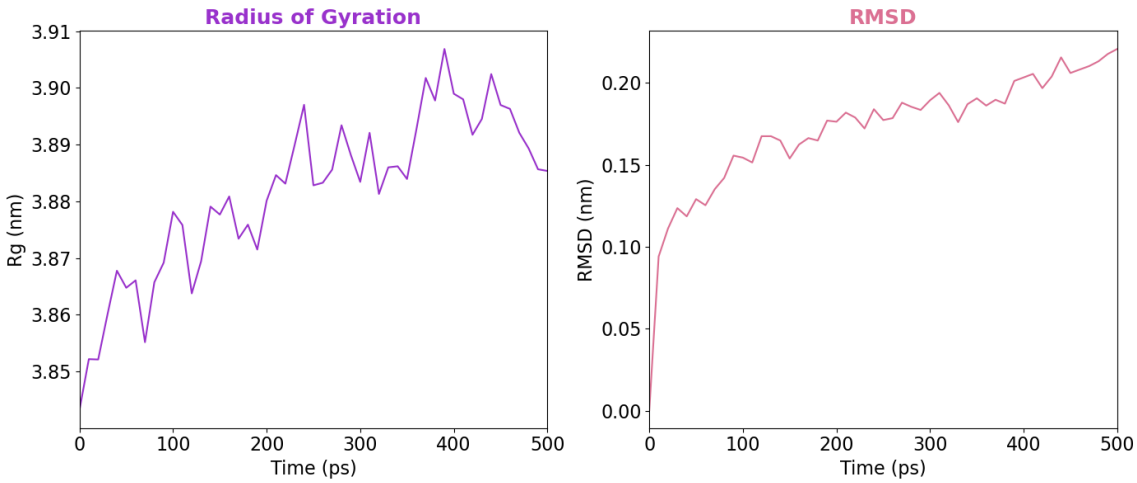

Figure A.3: **Structural evolution of BSA during a 500 ps molecular dynamics simulation.** The left panel shows the radius of gyration (R_g), which gradually increases over time, indicating slight conformational expansion. The right panel presents the root mean square deviation (RMSD), which steadily increases throughout the simulation, suggesting that the protein continues to undergo structural changes without fully stabilizing.

A.2 PR65 Supporting Information

A.2.1 PR65 in low concentration of SMAP

Using the NOT technique for the single-molecule binding assay at a reduced ligand concentration of 5 μM results in a lower frequency of binding events and decreased occupancy of the protein's higher scattering, elongated state. As shown in Figure A.4a, the trapping signal of PR65 protein differs with 20 μM and 5 μM concentrations of ATUX-8385, with the lower concentration exhibiting a prolonged duration in the more compact form. At lower ligand concentration ($5\mu M$), the frequency of binding events decreases compared to 20 μM (Figure **??**b). Specifically, at this reduced concentration (n=4), the protein spends 37% of its time in the elongated state, compared to 52% at 20 µM (n=8) (Figure A.4c). This difference allows us to identify the bound state as the more elongated form of the protein.

A.2.2 Binding constants of individual proteins

Table A.1: Table of ligand dissociation and association rate constants, dissociation constant, coefficient of determination, and duration of the trapped signal analyzed.

Protein	$\boldsymbol{k}_{\text{off}}$ (s^{-1})	$\boldsymbol{k}_{\text{on}}$ ($\text{s}^{-1}\mu\text{M}^{-1}$)	$\boldsymbol{K_D}$ (μM)	$\boldsymbol{R^2}_{\text{Bound}}$	$\boldsymbol{R^2}_{\text{Unbound}}$	**Total time analyzed (s)**
PR65 1	2.03	0.16	13.0	0.9885	0.9906	110
PR65 2	2.15	0.19	11.2	0.9834	0.9707	117
PR65 3	2.15	0.17	17.1	0.9838	0.9633	146
PR65 4	2.42	0.20	12.3	0.9884	0.9791	161
PR65 5	2.79	0.19	14.9	0.9749	0.9817	102
PR65 6	3.34	0.19	17.7	0.9625	0.9777	99
PR65 7	2.20	0.19	11.4	0.9769	0.9682	70
PR65 8	2.33	0.21	11.1	0.9636	0.9796	110

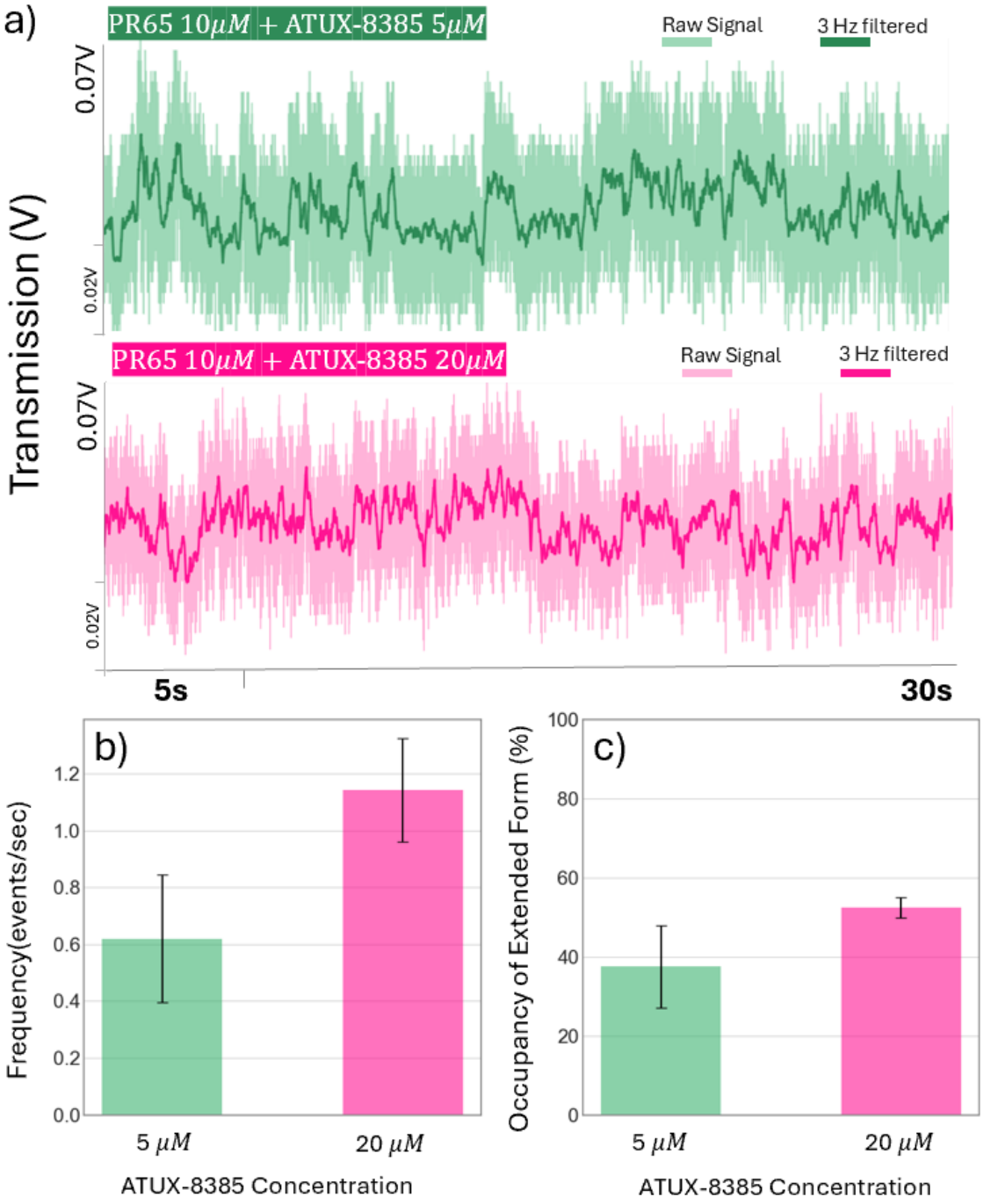

Figure A.4: **Comparison between low and high ATUX-8385 concentration** (a) Trapping signal of PR65 protein with 20 μM and 5 μM of ATUX-8385. Relative to high concentration of small molecule, the low concentration scattering signal exhibited a prolonged duration in the more compact form. (b) Bar plot comparison of frequency of binding events at a small molecule concentration of 20μM (n=8) and 5μM (n=4). At lower ligand concentration, a decrease in frequency (binding events per second) is observed. (b) At 20μM (n=8) of ligand, the protein on average exist in the elongated form 52% of a time whilst at a ligand concentration of 5μM(n=4), on average the protein exists in elongated form 37% of the time.

Bibliography

[1] Debabrata Goswami. Nobel prize in physics–2018. *Resonance*, 23:1333–1341, 2018.

[2] Hu Zhang and Kuo-Kang Liu. Optical tweezers for single cells. *Journal of the Royal Society interface*, 5(24):671–690, 2008.

[3] Karl J Aufderheide, Qing Du, and Edward S Fry. Directed positioning of micronuclei in paramecium tetraurelia with laser tweezers: Absence of detectible damage after manipulation. *Journal of Eukaryotic Microbiology*, 40(6):793–796, 1993.

[4] Yuanjie Pang and Reuven Gordon. Optical trapping of a single protein. *Nano Letters*, 12(1):402–406, January 2012.

[5] Arman Yousefi, Cuifeng Ying, Christopher D. J. Parmenter, Mahya Assadipapari, Gabriel Sanderson, Ze Zheng, Lei Xu, Saaman Zargarbashi, Graham J. Hickman, Richard B. Cousins, Christopher J. Mellor, Michael Mayer, and Mohsen Rahmani. Optical monitoring of in situ iron loading into single, native ferritin proteins. *Nano Letters*, 23(8):3251–3258, April 2023.

[6] Matthew Peters, Tianyu Zhao, Sherin George, Viet Giang Truong, Síle Nic Chormaic, Cuifeng Ying, René A. Nome, and Reuven Gordon. Energy landscape of conformational changes for a single unmodified protein. *Npj Biosensing*, 1(1):14, November 2024.

[7] Antoine M van Oijen. Single-molecule approaches to characterizing kinetics of biomolecular interactions. *Current Opinion in Biotechnology*, 22(1):75–80, February 2011.

[8] David S White, Mackinsey A Smith, Baron Chanda, and Randall H Goldsmith. Strategies for overcoming the single-molecule concentration barrier. *ACS Measurement Science Au*, 3(4):239–257, 2023.

[9] Harold P Erickson. Size and shape of protein molecules at the nanometer level determined by sedimentation, gel filtration, and electron microscopy. *Biological Procedures Online*, 11:32–51, 2009.

[10] Cansu Küey, Gabrielle Larocque, Nicholas I Clarke, and Stephen J Royle. Unintended perturbation of protein function using gfp nanobodies in human cells. *Journal of Cell Science*, 132(21):jcs234955, 2019.

[11] Fuming Zhang, Heather A Moniz, Benjamin Walcott, Kelley W Moremen, Lianchun Wang, and Robert J Linhardt. Probing the impact of gfp tagging on robo1-heparin interaction. *Glycoconjugate Journal*, 31:299–307, 2014.

[12] Arthur Ashkin, James M Dziedzic, John E Bjorkholm, and Steven Chu. Observation of a single-beam gradient force optical trap for dielectric particles. *Optics Letters*, 11(5):288–290, 1986.

[13] Arthur Ashkin. Acceleration and trapping of particles by radiation pressure. *Physical Review Letters*, 24(4):156–159, January 1970. Publisher: American Physical Society.

[14] Alessandro Magazzù and Carlos Marcuello. Investigation of soft matter nanomechanics by atomic force microscopy and optical tweezers: a comprehensive review. *Nanomaterials*, 13(6):963, January 2023. Number: 6 Publisher: Multidisciplinary Digital Publishing Institute.

[15] Marco Capitanio and Francesco S. Pavone. Interrogating biology with force: single molecule high-resolution measurements with optical tweezers. *Biophysical Journal*, 105(6):1293–1303, September 2013. Publisher: Elsevier.

[16] Peter J. Reece, Wen Jun Toe, Fan Wang, Suriati Paiman, Qiang Gao, H. Hoe Tan, and C. Jagadish. Characterization of semiconductor nanowires using optical tweezers. *Nano Letters*, 11(6):2375–2381, June 2011. Publisher: American Chemical Society.

[17] Praveenkumar Pinapati, Jostine Puthenveetil Joby, and Sudhir Cherukulappurath. Graphene oxide based two-dimensional optical tweezers for low power trapping of quantum dots and E. coli bacteria. *ACS Applied Nano Materials*, 3(6):5107–5115, June 2020. Publisher: American Chemical Society.

[18] Scot C. Kuo and Michael P. Sheetz. Force of single kinesin molecules measured with optical tweezers. *Science*, 260(5105):232–234, 1993. Publisher: American Association for the Advancement of Science.

[19] Carlos J. Bustamante, Yann R. Chemla, Shixin Liu, and Michelle D. Wang. Optical tweezers in single-molecule biophysics. *Nature Reviews Methods Primers*, 1(1):1–29, March 2021. Publisher: Nature Publishing Group.

[20] Yuanjie Pang. *Nanophotonics with subwavelength apertures: theories and applications*. PhD thesis, University of Victoria, 2012.

[21] Keir C. Neuman and Steven M. Block. Optical trapping. *The Review of Scientific Instruments*, 75(9):2787–2809, September 2004.

[22] Jürgen Renn. Einstein's invention of Brownian motion. *Annalen der Physik*, 517(S1):23–37, February 2005.

[23] Carlo Bradac. Nanoscale optical trapping: a review. *Advanced Optical Materials*, 6(12):1800005, 2018. _eprint: https://advanced.onlinelibrary.wiley.com/doi/pdf/10.1002/adom.201800005.

[24] Hans Albrecht Bethe. Theory of diffraction by small holes. *Physical Review*, 66(7-8):163, 1944.

[25] John Weiner. The physics of light transmission through subwavelength apertures and aperture arrays. *Reports on Progress in Physics*, 72(6):064401, 2009.

[26] Thomas W Ebbesen, Henri J Lezec, HF Ghaemi, Tineke Thio, and Peter A Wolff. Extraordinary optical transmission through sub-wavelength hole arrays. *Nature*, 391(6668):667–669, 1998.

[27] Reuven Gordon, David Sinton, Karen L Kavanagh, and Alexandre G Brolo. A new generation of sensors based on extraordinary optical transmission. *Accounts of Chemical Research*, 41(8):1049–1057, 2008.

[28] Domna G Kotsifaki and Síle Nic Chormaic. Plasmonic optical tweezers based on nanostructures: fundamentals, advances and prospects. *Nanophotonics*, 8(7):1227–1245, 2019.

[29] William L Barnes, Alain Dereux, and Thomas W Ebbesen. Surface plasmon subwavelength optics. *Nature*, 424(6950):824–830, 2003.

[30] Mathieu L. Juan, Maurizio Righini, and Romain Quidant. Plasmon nano-optical tweezers. *Nature Photonics*, 5(6):349–356, June 2011.

[31] Mark I Stockman. Nanofocusing of optical energy in tapered plasmonic waveguides. *Physical Review Letters*, 93(13):137404, 2004.

[32] Nathan C Lindquist, Timothy W Johnson, Prashant Nagpal, David J Norris, and Sang-Hyun Oh. Plasmonic nanofocusing with a metallic pyramid and an integrated c-shaped aperture. *Scientific Reports*, 3(1):1857, 2013.

[33] Ardash Lalitha Ravindranath. *Double-nanohole optical trapping: fabrication and experimental methods*. PhD thesis, University of Victoria, 2019.

[34] Yuanyuan Chen, Abhay Kotnala, Li Yu, Jiasen Zhang, and Reuven Gordon. Wedge and gap plasmonic resonances in double nanoholes. *Optics Express*, 23(23):30227–30236, 2015.

[35] Seung Ju Yoon, Jungmin Lee, Sangyoon Han, Chang-Kyu Kim, Chi Won Ahn, Myung-Ki Kim, and Yong-Hee Lee. Non-fluorescent nanoscopic monitoring of a single trapped nanoparticle via nonlinear point sources. *Nature Communications*, 9(1):2218, 2018.

[36] Yuxin Zheng, Jason Ryan, Paul Hansen, Yao-Te Cheng, Tsung-Ju Lu, and Lambertus Hesselink. Nano-optical conveyor belt, part ii: demonstration of handoff between near-field optical traps. *Nano Letters*, 14(6):2971–2976, 2014.

[37] Mathieu L. Juan, Reuven Gordon, Yuanjie Pang, Fatima Eftekhari, and Romain Quidant. Self-induced back-action optical trapping of dielectric nanoparticles. *Nature Physics*, 5(12):915–919, December 2009.

[38] Zohreh Sharifi, Michael Dobinson, Ghazal Hajisalem, Mirali Seyed Shariatdoust, Adriaan L Frencken, Frank CJM van Veggel, and Reuven Gordon. Isolating and enhancing single-photon emitters for 1550 nm quantum light sources us-

ing double nanohole optical tweezers. *The Journal of Chemical Physics*, 154(18), 2021.

[39] Elham Hosseini Toodeshki, Adriaan L. Frencken, Frank C. J. M. van Veggel, and Reuven Gordon. Thermometric analysis of nanoaperture-trapped erbium-containing nanocrystals. *ACS Photonics*, 11(4):1390–1395, April 2024.

[40] Giorgio Volpe and Giovanni Volpe. Simulation of a brownian particle in an optical trap. *American Journal of Physics*, 81(3):224–230, 2013.

[41] Yonggun Jun, Suvranta K Tripathy, Babu RJ Narayanareddy, Michelle K Mattson-Hoss, and Steven P Gross. Calibration of optical tweezers for in vivo force measurements: how do different approaches compare? *Biophysical Journal*, 107(6):1474–1484, 2014.

[42] Kirstine Berg-Sørensen and Henrik Flyvbjerg. Power spectrum analysis for optical tweezers. *Review of Scientific Instruments*, 75(3):594–612, 2004.

[43] Abhay Kotnala and Reuven Gordon. Quantification of high-efficiency trapping of nanoparticles in a double nanohole optical tweezer. *Nano Letters*, 14(2):853–856, 2014.

[44] Skyler Wheaton and Reuven Gordon. Molecular weight characterization of single globular proteins using optical nanotweezers. *Analyst*, 140(14):4799–4803, June 2015.

[45] Adarsh Lalitha Ravindranath, Mirali Seyed Shariatdoust, Samuel Mathew, and Reuven Gordon. Colloidal lithography double-nanohole optical trapping of nanoparticles and proteins. *Optics Express*, 27(11):16184–16194, May 2019.

[46] Quanbo Jiang, Benoît Rogez, Jean-Benoît Claude, Antonin Moreau, Julien Lumeau, Guillaume Baffou, and Jérôme Wenger. Adhesion layer influence on controlling the local temperature in plasmonic gold nanoholes. *Nanoscale*, 12(4):2524–2531, 2020.

[47] Burak T. Kaynak, Zakaria L. Dahmani, Pemra Doruker, Anupam Banerjee, Shang-Hua Yang, Reuven Gordon, Laura S. Itzhaki, and Ivet Bahar. Cooperative mechanics of PR65 scaffold underlies the allosteric regulation of the phosphatase PP2A. *Structure*, 31(5):607–618.e3, May 2023.

[48] Parthasarathy Seshacharyulu, Poomy Pandey, Kaustubh Datta, and Surinder K. Batra. Phosphatase: PP2A structural importance, regulation and its aberrant expression in cancer. *Cancer Letters*, 335(1):9–18, July 2013.

[49] Jason D Arroyo and William C Hahn. Involvement of pp2a in viral and cellular transformation. *Oncogene*, 24(52):7746–7755, 2005.

[50] Sahar Mazhar, Sarah E Taylor, Jaya Sangodkar, and Goutham Narla. Targeting pp2a in cancer: Combination therapies. *Biochimica et Biophysica Acta (BBA)-Molecular Cell Research*, 1866(1):51–63, 2019.

[51] Melissa R Junttila, Pietri Puustinen, Minna Niemelä, Raija Ahola, Hugh Arnold, Trine Böttzauw, Risto Ala-aho, Christina Nielsen, Johanna Ivaska, Yoichi Taya, et al. Cip2a inhibits pp2a in human malignancies. *Cell*, 130(1):51–62, 2007.

[52] Anna A Sablina, Melissa Hector, Nathalie Colpaert, and William C Hahn. Identification of pp2a complexes and pathways involved in cell transformation. *Cancer Research*, 70(24):10474–10484, 2010.

[53] Caitlin M O'Connor, Abbey Perl, Daniel Leonard, Jaya Sangodkar, and Goutham Narla. Therapeutic targeting of pp2a. *The international Journal of Biochemistry & Cell Biology*, 96:182–193, 2018.

[54] Jaya Sangodkar, Caroline C Farrington, Kimberly McClinch, Matthew D Galsky, David B Kastrinsky, and Goutham Narla. All roads lead to pp 2a: exploiting the therapeutic potential of this phosphatase. *The FEBS Journal*, 283(6):1004–1024, 2016.

[55] Laura V. Bownes, Janet R. Julson, Colin H. Quinn, Sara Claire Hutchins, Michael H. Erwin, Hooper R. Markert, Jerry E. Stewart, Elizabeth Mroczek-Musulman, Jamie Aye, Karina J. Yoon, Michael Ohlmeyer, and Elizabeth A. Beierle. The effects of protein phosphatase 2A activation with novel tricyclic sulfonamides on hepatoblastoma. *Journal of Pediatric Surgery*, 58(6):1145–1154, June 2023.

[56] Jaya Sangodkar, Abbey Perl, Rita Tohme, Janna Kiselar, David B Kastrinsky, Nilesh Zaware, Sudeh Izadmehr, Sahar Mazhar, Danica D Wiredja, Caitlin M O'Connor, Divya Hoon, Neil S Dhawan, Daniela Schlatzer, Shen Yao, Daniel

Leonard, Alain C Borczuk, Giridharan Gokulrangan, Lifu Wang, Elena Svenson, Caroline C Farrington, Eric Yuan, Rita A Avelar, Agnes Stachnik, Blake Smith, Vickram Gidwani, Heather M Giannini, Daniel McQuaid, Kimberly McClinch, Zhizhi Wang, Alice C Levine, Rosalie C Sears, Edward Y Chen, Qiaonan Duan, Manish Datt, Shozeb Haider, Avi Ma'ayan, Analisa DiFeo, Neelesh Sharma, Matthew D Galsky, David L Brautigan, Yiannis A Ioannou, Wenqing Xu, Mark R Chance, Michael Ohlmeyer, and Goutham Narla. Activation of tumor suppressor protein PP2A inhibits KRAS-driven tumor growth. *The Journal of Clinical Investigation*, 127(6):2081–2090, June 2017.

[57] Alison Grinthal, Ivana Adamovic, Beth Weiner, Martin Karplus, and Nancy Kleckner. PR65, the HEAT-repeat scaffold of phosphatase PP2A, is an elastic connector that links force and catalysis. *Proceedings of the National Academy of Sciences*, 107(6):2467–2472, February 2010.

[58] Ahmed A. Al Balushi and Reuven Gordon. A label-free untethered approach to single-molecule protein binding kinetics. *Nano Letters*, 14(10):5787–5791, October 2014.

[59] Ahmed A. Al Balushi, Abhay Kotnala, Skyler Wheaton, Ryan M. Gelfand, Yashaswini Rajashekara, and Reuven Gordon. Label-free free-solution nanoaperture optical tweezers for single molecule protein studies. *Analyst*, 140(14):4760–4778, 2015.

[60] Russell A. Jensen, I-Chun Huang, Ou Chen, Jennifer T. Choy, Thomas S. Bischof, Marko Lončar, and Moungi G. Bawendi. Optical trapping and two-photon excitation of colloidal quantum dots using bowtie apertures. *ACS Photonics*, 3(3):423–427, March 2016.

[61] Chuchuan Hong, Sen Yang, and Justus C. Ndukaife. Stand-off trapping and manipulation of sub-10 nm objects and biomolecules using opto-thermo-electrohydrodynamic tweezers. *Nature Nanotechnology*, 15(11):908–913, November 2020.

[62] Shiyun Lin and Kenneth B. Crozier. Trapping-assisted sensing of particles and proteins using on-chip optical microcavities. *ACS Nano*, 7(2):1725–1730, February 2013.

[63] Chang Chen, Mathieu L. Juan, Yi Li, Guido Maes, Gustaaf Borghs, Pol Van Dorpe, and Romain Quidant. Enhanced optical trapping and arrangement of nano-objects in a plasmonic nanocavity. *Nano Letters*, 12(1):125–132, January 2012.

[64] Seung Ju Yoon, Da In Song, Jungmin Lee, Myung-Ki Kim, Yong-Hee Lee, and Chang-Kyu Kim. Hopping of single nanoparticles trapped in a plasmonic double-well potential. *Nanophotonics*, 9(16):4729–4735, November 2020.

[65] Abhay Kotnala, Pavana Siddhartha Kollipara, Jingang Li, and Yuebing Zheng. Overcoming diffusion-limited trapping in nanoaperture tweezers using opto-thermal-induced flow. *Nano Letters*, 20(1):768–779, January 2020.

[66] Daehan Yoo, Kargal L. Gurunatha, Han-Kyu Choi, Daniel A. Mohr, Christopher T. Ertsgaard, Reuven Gordon, and Sang-Hyun Oh. Low-power optical trapping of nanoparticles and proteins with resonant coaxial nanoaperture using 10 nm gap. *Nano Letters*, 18(6):3637–3642, June 2018.

[67] Domna G. Kotsifaki, Viet Giang Truong, and Síle Nic Chormaic. Fano-resonant, asymmetric, metamaterial-assisted tweezers for single nanoparticle trapping. *Nano Letters*, 20(5):3388–3395, May 2020.

[68] Sai Santosh Sasank Peri, Manoj Kumar Sabnani, Muhammad Usman Raza, Elizabeth L. Urquhart, Soroush Ghaffari, Jung Soo Lee, Min Jun Kim, Jon Weidanz, and George Alexandrakis. Quantification of low affinity binding interactions between natural killer cell inhibitory receptors and targeting ligands with a self-induced back-action actuated nanopore electrophoresis (SANE) sensor. *Nanotechnology*, 32(4):045501, October 2020.

[69] Maxim Belkin, Shu-Han Chao, Magnus P. Jonsson, Cees Dekker, and Aleksei Aksimentiev. Plasmonic nanopores for trapping, controlling displacement, and sequencing of DNA. *ACS Nano*, 9(11):10598–10611, November 2015.

[70] Quanbo Jiang, Benoît Rogez, Jean-Benoît Claude, Guillaume Baffou, and Jérôme ger. Quantifying the role of the surfactant and the thermophoretic force in plasmonic nano-optical trapping. *Nano Letters*, 20(12):8811–8817, December 2020.

[71] Muhammad Usman Raza, Sai Santosh Sasank Peri, Liang-Chieh Ma, Samir M Iqbal, and George Alexandrakis. Self-induced back action actuated nanopore electrophoresis (sane). *Nanotechnology*, 29(43):435501, 2018.

[72] Daniel Verschueren, Xin Shi, and Cees Dekker. Nano-optical tweezing of single proteins in plasmonic nanopores. *Small Methods*, 3(5):1800465, 2019.

[73] Sai Santosh Sasank Peri, Manoj K Sabnani, Muhammad Usman Raza, Soroush Ghaffari, Susanne Gimlin, Debra D Wawro, Jung Soo Lee, Min Jun Kim, Jon Weidanz, and George Alexandrakis. Detection of specific antibody-ligand interactions with a self-induced back-action actuated nanopore electrophoresis sensor. *Nanotechnology*, 31(8):085502, 2019.

[74] Wayne Yang, Madeleine van Dijk, Christian Primavera, and Cees Dekker. Fib-milled plasmonic nanoapertures allow for long trapping times of individual proteins. *Iscience*, 24(11), 2021.

[75] Anupam Banerjee, Samuel Mathew, Mohsin M. Naqvi, Sema Z. Yilmaz, Maria Zacharopoulou, Pemra Doruker, Janet R. Kumita, Shang-Hua Yang, Mert Gur, Laura S. Itzhaki, Reuven Gordon, and Ivet Bahar. Influence of point mutations on PR65 conformational adaptability: Insights from molecular simulations and nanoaperture optical tweezers. *Science Advances*, 10(22):eadn2208, May 2024.

[76] Ahmed A Al Balushi and Reuven Gordon. Label-free free-solution single-molecule protein–small molecule interaction observed by double-nanohole plasmonic trapping. *ACS Photonics*, 1(5):389–393, 2014.

[77] Priyanka Sandal, Chian Ju Jong, Ronald A. Merrill, Jianing Song, and Stefan Strack. Protein phosphatase 2A – structure, function and role in neurodevelopmental disorders. *Journal of Cell Science*, 134(13), July 2021.

[78] Hirota Fujiki, Eisaburo Sueoka, Tatsuro Watanabe, Atsumasa Komori, and Masami Suganuma. Cancer progression by the okadaic acid class of tumor promoters and endogenous protein inhibitors of PP2A, SET and CIP2A. *Journal of Cancer Research and Clinical Oncology*, 149(11):9425–9433, 2023.

[79] George A Calin, Maria Grazia di Iasio, Elisabetta Caprini, Igor Vorechovsky, Pier Giorgio Natali, Gabriella Sozzi, Carlo M Croce, Giuseppe Barbanti-Brodano, Giandomenico Russo, and Massimo Negrini. Low frequency of alter-

ations of the α (PPP2R1A) and β (PPP2R1B) isoforms of the subunit A of the serine-threonine phosphatase 2A in human neoplasms. *Oncogene*, 19(9):1191–1195, February 2000.

[80] Madhumathi Gnanaprakash, Agnieszka Staniszewski, Hong Zhang, Rose Pitstick, Michael P. Kavanaugh, Ottavio Arancio, and Russell E. Nicholls. Leucine Carboxyl Methyltransferase 1 Overexpression Protects Against Cognitive and Electrophysiological Impairments in Tg2576 APP Transgenic Mice. *Journal of Alzheimer's Disease*, 79(4):1813–1829, February 2021.

[81] Wilco Nijenhuis, Giulia Vallardi, Antoinette Teixeira, Geert J. P. L. Kops, and Adrian T. Saurin. Negative feedback at kinetochores underlies a responsive spindle checkpoint signal. *Nature Cell Biology*, 16(12):1257–1264, December 2014. Publisher: Nature Publishing Group.

[82] Ralf Ruediger, Jill E Van Wart Hood, Marc Mumby, and Gernot Walter. Constant expression and activity of protein phosphatase 2a in synchronized cells. *Molecular and Cellular Biology*, 11(8):4282–4285, 1991.

[83] Daniel Leonard, Wei Huang, Sudeh Izadmehr, Caitlin M. O'Connor, Danica D. Wiredja, Zhizhi Wang, Nilesh Zaware, Yinghua Chen, Daniela M. Schlatzer, Janna Kiselar, Nikhil Vasireddi, Stefan Schüchner, Abbey L. Perl, Matthew D. Galsky, qing Xu, David L. Brautigan, Egon Ogris, Derek J. Taylor, and Goutham Narla. Selective PP2A enhancement through biased heterotrimer stabilization. *Cell*, 181(3):688–701.e16, April 2020.

[84] Caitlin M. O'Connor, Abbey Perl, Daniel Leonard, Jaya Sangodkar, and Goutham Narla. Therapeutic targeting of PP2A. *The International Journal of Biochemistry & Cell Biology*, 96:182–193, March 2018.

[85] Martin C. S. Wong, Johnny Y. Jiang, William B. Goggins, Miaoyin Liang, Yuan Fang, Franklin D. H. Fung, Colette Leung, Harry H. X. Wang, Grace L. H. Wong, Vincent W. S. Wong, and Henry L. Y. Chan. International incidence and mortality trends of liver cancer: a global profile. *Scientific Reports*, 7(1):45846, March 2017. Publisher: Nature Publishing Group.

[86] Hashem B. El-Serag and Andrew C. Mason. Risk factors for the rising rates of primary liver cancer in the United States. *Archives of Internal Medicine*, 160(21):3227–3230, November 2000.

[87] David Anwanwan, Santosh Kumar Singh, Shriti Singh, Varma Saikam, and Rajesh Singh. Challenges in liver cancer and possible treatment approaches. *Biochimica et Biophysica Acta (BBA) - Reviews on Cancer*, 1873(1):188314, January 2020.

[88] Ming Hui Chen, Risto Kerkelä, and Thomas Force. Mechanisms of cardiac dysfunction associated with tyrosine kinase inhibitor cancer therapeutics. *Circulation*, 118(1):84–95, 2008.

[89] Amit Arora and Eric M Scholar. Role of tyrosine kinase inhibitors in cancer therapy. *The Journal of Pharmacology and Experimental Therapeutics*, 315(3):971–979, 2005.

[90] Neil Vasan, José Baselga, and David M Hyman. A view on drug resistance in cancer. *Nature*, 575(7782):299–309, 2019.

[91] Scott A Hollingsworth and Ron O Dror. Molecular dynamics simulation for all. *Neuron*, 99(6):1129–1143, 2018.

[92] Scott E Feller. Molecular dynamics simulations as a complement to nuclear magnetic resonance and x-ray diffraction measurements. *Methods in Membrane Lipids*, pages 89–102, 2007.

[93] Michael P Allen et al. Introduction to molecular dynamics simulation. *Computational Soft Matter: From Synthetic Polymers to Proteins*, 23(1):1–28, 2004.

[94] Olgun Guvench and Alexander D MacKerell Jr. Comparison of protein force fields for molecular dynamics simulations. *Molecular Modeling of Proteins*, pages 63–88, 2008.

[95] GROMACS Development Team. Gromacs 2020.6 user guide: Force fields, 2020. Accessed: 28-Feb-2025.

[96] Weiguo Liu, Bertil Schmidt, Gerrit Voss, and Wolfgang Müller-Wittig. Accelerating molecular dynamics simulations using graphics processing units with cuda. *Computer Physics Communications*, 179(9):634–641, 2008.

[97] Jens Glaser, Trung Dac Nguyen, Joshua A Anderson, Pak Lui, Filippo Spiga, Jaime A Millan, David C Morse, and Sharon C Glotzer. Strong scaling of

general-purpose molecular dynamics simulations on gpus. *Computer Physics Communications*, 192:97–107, 2015.

[98] Samuel Mathew and Reuven Gordon. Self-induced back-action for aperture trapping: Bethe-Rayleigh theory. *Optics Express*, 31(26):44190–44198, December 2023.

[99] Noa Hacohen, Candice JX Ip, and Reuven Gordon. Analysis of egg white protein composition with double nanohole optical tweezers. *ACS Omega*, 3(5):5266–5272, 2018.

[100] Cuifeng Ying, Edona Karakaçi, Esteban Bermúdez-Ureña, Alessandro Ianiro, Saurabh Awasthi, Anirvan Guha, Louise Bryan, Jonathan List, Sandor Balog, Guillermo P Acuna, Reuven Gordon, and Michael Mayer. Watching single unmodified enzymes at work. *arXiv*, 2021.

[101] Larnii S Booth, Eloise V Browne, Nicolas P Mauranyapin, Lars S Madsen, Shelley Barfoot, Alan Mark, and Warwick P Bowen. Modelling of the dynamic polarizability of macromolecules for single-molecule optical biosensing. *Scientific Reports*, 12(1):1995, 2022.

[102] Samuel DeLuca, Karen Khar, and Jens Meiler. Fully flexible docking of medium sized ligand libraries with RosettaLigand. *Plos One*, 10(7):e0132508, July 2015.

[103] Sergey Lyskov, Fang-Chieh Chou, Shane Ó Conchúir, Bryan S. Der, Kevin Drew, Daisuke Kuroda, Jianqing Xu, Brian D. Weitzner, P. Douglas Renfrew, Parin Sripakdeevong, Benjamin Borgo, James J. Havranek, Brian Kuhlman, Tanja Kortemme, Richard Bonneau, Jeffrey J. Gray, and Rhiju Das. Serverification of molecular modeling applications: The Rosetta online erver that includes everyone (ROSIE). *Plos One*, 8(5):e63906, May 2013.

[104] Anna Vangone, Joerg Schaarschmidt, Panagiotis Koukos, Cunliang Geng, Nevia Citro, Mikael E Trellet, Li C Xue, and Alexandre M J J Bonvin. Large-scale prediction of binding affinity in protein–small ligand complexes: the PRODIGY-LIG web server. *Bioinformatics*, 35(9):1585–1587, May 2019.

[105] Garrett M. Morris, Ruth Huey, William Lindstrom, Michel F. Sanner, Richard K. Belew, David S. Goodsell, and Arthur J. Olson. AutoDock4 and

AutoDockTools4: Automated docking with selective receptor flexibility. *Journal of Computational Chemistry*, 30(16):2785–2791, 2009.

[106] Quanbo Jiang, Benoît Rogez, Jean-Benoît Claude, Guillaume Baffou, and Jérôme Wenger. Temperature measurement in plasmonic nanoapertures used for optical trapping. *ACS Photonics*, 6(7):1763–1773, July 2019.

[107] Marie Synakewicz, Daniela Bauer, Matthias Rief, and Laura S. Itzhaki. Bioorthogonal protein-DNA conjugation methods for force spectroscopy. *Scientific Reports*, 9(1):13820, September 2019.

[108] Ghazal Hajisalem, Elham Babaei, Michael Dobinson, Shohei Iwamoto, Zohreh Sharifi, Jon Eby, Marie Synakewicz, Laura S Itzhaki, and Reuven Gordon. Accessible high-performance double nanohole tweezers. *Optics Express*, 30(3):3760–3769, 2022.

[109] Jonathan E. Bronson, Jingyi Fei, Jake M. Hofman, Ruben L. Gonzalez, and Chris H. Wiggins. Learning rates and states from biophysical time series: A Bayesian approach to model selection and single-molecule FRET data. *Biophysical Journal*, 97(12):3196–3205, December 2009.

[110] Jerome Eberhardt, Diogo Santos-Martins, Andreas F. Tillack, and Stefano Forli. AutoDock Vina 1.2.0: new docking methods, expanded force field, and Python bindings. *Journal of Chemical Information and Modeling*, 61(8):3891–3898, August 2021.

[111] William L Jorgensen, Jayaraman Chandrasekhar, Jeffry D Madura, Roger W Impey, and Michael L Klein. Comparison of simple potential functions for simulating liquid water. *The Journal of Chemical Physics*, 79(2):926–935, 1983.

[112] William Humphrey, Andrew Dalke, and Klaus Schulten. VMD: Visual molecular dynamics. *Journal of Molecular Graphics*, 14(1):33–38, February 1996.

[113] James C. Phillips, David J. Hardy, Julio D. C. Maia, John E. Stone, João V. Ribeiro, Rafael C. Bernardi, Ronak Buch, Giacomo Fiorin, Jérôme Hénin, Wei Jiang, Ryan McGreevy, Marcelo C. R. Melo, Brian K. Radak, Robert D. Skeel, Abhishek Singharoy, Yi Wang, Benoît Roux, Aleksei Aksimentiev, Zaida Luthey-Schulten, Laxmikant V. Kalé, Klaus Schulten, Christophe Chipot, and

Emad Tajkhorshid. Scalable molecular dynamics on CPU and GPU architectures with NAMD. *The Journal of Chemical Physics*, 153(4):044130, July 2020.

[114] Robert B. Best, Xiao Zhu, Jihyun Shim, Pedro E. M. Lopes, Jeetain Mittal, Michael Feig, and Alexander D. Jr. MacKerell. Optimization of the additive CHARMM all-atom protein force field targeting improved sampling of the backbone ϕ, ψ and side-chain $\chi 1$ and $\chi 2$ dihedral angles. *Journal of Chemical Theory and Computation*, 8(9):3257–3273, September 2012.

[115] Jaime Ortega-Arroyo and Philipp Kukura. Interferometric scattering microscopy (iscat): new frontiers in ultrafast and ultrasensitive optical microscopy. *Physical Chemistry Chemical Physics*, 14(45):15625–15636, 2012.

[116] Daniel Cole, Gavin Young, Alexander Weigel, Aleksandar Sebesta, and Philipp Kukura. Label-free single-molecule imaging with numerical-aperture-shaped interferometric scattering microscopy. *ACS Photonics*, 4(2):211–216, 2017.

[117] Daniel Branton, David W Deamer, Andre Marziali, Hagan Bayley, Steven A Benner, Thomas Butler, Massimiliano Di Ventra, Slaven Garaj, Andrew Hibbs, Xiaohua Huang, et al. The potential and challenges of nanopore sequencing. *Nature Biotechnology*, 26(10):1146–1153, 2008.

[118] Yunhao Wang, Yue Zhao, Audrey Bollas, Yuru Wang, and Kin Fai Au. Nanopore sequencing technology, bioinformatics and applications. *Nature Biotechnology*, 39(11):1348–1365, 2021.

[119] Scot C Kuo and Michael P Sheetz. Force of single kinesin molecules measured with optical tweezers. *Science*, 260(5105):232–234, 1993.

[120] Yanhua Wu, Dong Sun, and Wenhao Huang. Mechanical force characterization in manipulating live cells with optical tweezers. *Journal of Biomechanics*, 44(4):741–746, 2011.

[121] Ana Zehtabi-Oskuie, Hao Jiang, Bryce R Cyr, Douglas W Rennehan, Ahmed A Al-Balushi, and Reuven Gordon. Double nanohole optical trapping: dynamics and protein-antibody co-trapping. *Lab on a Chip*, 13(13):2563–2568, 2013.

[122] Zhenglong Li, Niranjan Haridas, Sreerag Kaaliveetil, Yu-Hsuan Cheng, Charmi Chande, Veronica Perez, Amir K Miri, and Sagnik Basuray. Low-cost rapid

prototyping for microfluidics using parafilm®-based microchannels for low resource settings. *Sensors and Actuators B: Chemical*, 404:135212, 2024.